

Equatorial wave structure and momentum budget of the Madden-Julian Oscillation

Jialin Lin¹, Minghua Zhang² and Brian Mapes¹

¹ NOAA-CIRES Climate Diagnostics Center, Boulder, CO 80305

² State University of New York, Stony Brook, NY 11794

July, 2003

ABSTRACT

In theoretical studies of the Madden-Julian Oscillation (MJO), the zonal momentum equation is often linearized about a state at rest. The resultant balance at the equator is between local tendency and pressure gradient force, implying an in-phase relationship between zonal wind and geopotential height. However, the observed equatorial wave structure of the MJO shows a quarter cycle phase difference between zonal wind and geopotential height, suggesting that other terms also contribute to the zonal momentum budget. Direct calculation of zonal momentum budget reveals that the dominant balance at the equator is actually between the advective tendency and pressure gradient force. The local tendency is small, as well as the convective momentum flux convergence suggested by budget residual. The advective tendency is dominated by the linear terms associated with time-mean zonal and vertical motions. Simple scaling analysis shows that over the warm pool region, the time-mean upper-level upward motion, zonal divergence, and easterly wind are bound to cause an advective tendency much larger than the local tendency at the MJO time-scale. Therefore, linear advection terms associated with time-mean flow must be included when modeling the MJO wave structure.

1. Introduction

Discovered by Madden and Julian (1971, 1972), the Madden-Julian Oscillation (MJO) is one of the dominant intraseasonal large-scale disturbances in the tropics (e.g. Weickmann et al. 1985, Lau and Chan 1985, Salby and Hendon 1994, Wheeler and Kiladis 1999). It affects a wide range of tropical weather such as the onset and breaks of the Indian and Australian summer monsoons (e.g. Yasunari 1979, Hendon and Liebmann 1990), and the formation of tropical cyclones (e.g. Nakazawa 1986, Liebmann et al. 1994). It also drives teleconnections to the extratropics (e.g., Lau and Phillips 1986) and impacts some important extratropical weather. On a longer timescale, the MJO is observed to trigger or terminate some El Nino events (e.g. Kessler et al. 1995, Takayabu et al. 1999, Bergman et al. 2001). Therefore, the MJO is important for both extended-range weather forecasting and long-term climate prediction.

Matsuno (1966) and Lindzen (1967) first developed the linear perturbation theory for large-scale equatorial disturbances. The momentum equation was linearized about an atmosphere at rest, i.e. neglecting the linear advection terms associated with basic flow, the nonlinear advection terms, and the convective momentum flux convergence. The solutions included Kelvin, equatorial Rossby, mixed Rossby-gravity, eastward inertio-gravity, and westward inertio-gravity waves. Because observations show that the MJO propagates eastward and the meridional wind anomaly is small near the equator (e.g. Madden and Julian 1971, 1972, Knutson and Weickmann 1987, Hendon and Salby 1994), the equatorial wave structure of the MJO is often considered as

a Kelvin wave, which is schematically shown in Fig. 1. Therefore, a Kelvin-wave model is often used for studying different wave-convection feedback mechanisms in the MJO, such as the wave-CISK (Convective Instability of the Second Kind) mechanism (e.g. Lau and Peng 1987, Chang and Lim 1988, Crum and Dunkerton 1992), the frictional wave-CISK mechanism (e.g. Wang 1988), the WISHE (Wave Induced Surface Heat Exchange) mechanism (e.g. Emanuel 1987, Neelin et al. 1987), the phase-lagged wave-CISK mechanism (e.g. Cho et al. 1994), and the phase-lagged WISHE mechanism (e.g. Emanuel 1993, Neelin and Yu 1994).

However, several characteristics of the observed MJO raised the question whether it is really a Kelvin wave, or a completely different identity. The first characteristic is the dispersion relation. Wheeler and Kiladis (1999) presented a plot of the variance of near-equatorial outgoing longwave radiation (OLR) as a function of frequency and zonal wavenumber. After removing a red-noise background, these plots showed all of the equatorial wave modes predicted by Matsuno (1966) and Lindzen (1967). However, the MJO appeared as a distinct mode separated from the Kelvin mode, with a fixed frequency independent of wavenumber. This contrasts with the dispersion relation of the Kelvin wave in which frequency is proportional to wavenumber.

The second characteristic is the phase difference between zonal wind and geopotential height. If the zonal momentum equation is linearized about an atmosphere at rest, neglecting damping, then the balance at the equator is simply between the local tendency and the pressure gradient force. If the disturbance is neutral and has a well-defined phase speed, then zonal wind u and geopotential height Z at the equator will

be in phase for eastward-propagating disturbances and out of phase for westward-propagating disturbances. This was confirmed in observation for the Kelvin wave (Wheeler et al. 2000), the equatorial Rossby wave (Kiladis and Wheeler 1995), and the westward inertio-gravity wave (Heartel and Kiladis 2003). However, for the MJO, Madden and Julian (1972) found the lower troposphere u and Z have a quarter-cycle phase difference at a western Pacific station, suggesting that some terms other than the local tendency or pressure gradient force also contribute to the zonal momentum budget. Chang (1977) assumed that the “extra” term is convective momentum flux convergence, and developed a viscous Kelvin-wave theory of the MJO.

Because the MJO has larger signals in the upper troposphere than in the lower troposphere, the u - Z phase relationship in the upper troposphere is more important. Only a few observational studies analysed this phase relation (Hendon and Salby 1994, Kiladis and Weickmann 1992, Hsu 1996), and they showed inconsistent results. Hendon and Salby (1994) found that as the MJO moves eastward from the western Indian Ocean to the central Pacific Ocean, the MSU channel 2 temperature, representing troposphere mean temperature, is always nearly in phase with the 200 mb zonal wind, suggesting an u - Z in-phase relationship at the upper levels. On the contrary, Kiladis and Weickmann (1992) and Hsu (1996) found that in the western Pacific, the 200 mb geopotential height from operational analysis data lags the zonal wind by a quarter cycle.

In order to know whether the observed MJO is a Kelvin wave, in this study we use the in situ sounding data to check which of the above two results is correct. Madden

and Julian (1971, 1972, 1994) and Nishi (1989) used the sounding data to calculate the u - Z phase difference, but as reviewed by Madden and Julian (1994), the results were complex. Their method was somehow different from the above three papers (Hendon and Salby 1994, Kiladis and Weickmann 1992, Hsu 1996) which used deep convection as the reference time series. In order to compare with the results of Hendon and Salby (1994), Kiladis and Weickmann (1992), and Hsu (1996), in this study we used deep convection as the reference time series. We found a quarter cycle phase difference between u and Z in the upper troposphere, suggesting that the observed MJO is different from a Kelvin wave, and some “extra” terms do contribute to the zonal momentum budget.

In order to know exactly what the “extra” terms are, we further calculated the zonal momentum budget of the MJO. Previous studies calculated the momentum budget for mesoscale convective systems (Gallus and Johnson 1992, Wu and Yanai 1994, Mapes and Wu 2001), easterly waves (Stevens 1979), and seasonal mean of tropical atmosphere (Carr and Bretherton 2001). However, no calculation was done for the MJO. In this study, we calculated the budget using NCEP and ECMWF re-analysis data. The main budget uncertainties associated with pressure gradient forces and advection terms are reduced by (1) comparing between NCEP and ECMWF re-analyses, whose consistencies gave us more confidence, and (2) constructing long-term (15 years) MJO composite and considering only the statistically significant signals, which are likely real signals unless there are systematic errors coherent with the MJO. The results indicate that the extra terms are the linear advection terms associated

with background zonal and vertical motions, which largely balance the pressure gradient force. The local tendency is small, as well as the nonlinear advection terms and the convective momentum flux convergence. Therefore, the observed MJO is a mode different from the Kelvin wave, and the linear advection terms associated with time-mean flow must be included when modeling the MJO wave structure.

The datasets used in this study are described in section 2. Methods are described in section 3. The observed MJO wave structure is described in section 4. The zonal momentum budget is reported in section 5. Summary and discussions are given in section 6.

2. Data

The datasets used include:

- (1) 21 years (1979-1999) of twice daily upper air sounding data from tropical stations Chuuk, Pohnpei, and Honiara (Fig. 2). The variables used include wind, geopotential height and temperature at 12 mandatory levels. We average the data at each station to pentad data. There are only a few missing data, and they are filled with linear interpolation.
- (2) Three years (2000-2002) of twice daily upper air sounding data from Manus Island (Fig. 2) measured by the Atmospheric Radiation Measurement (ARM) project. The variables used include wind, geopotential height and temperature at two seconds vertical resolution. We average the data to pentad data. There are only a few missing data, and they are filled with linear interpolation.

(3) 21 years (1979-1999) of daily NCEP reanalysis data. The variables used include upper air wind, geopotential height, and temperature. The horizontal resolution is 2.5 degree longitude by 2.5 degree latitude. We average the data along the equator (between 5N and 5S) to pentad data with a zonal resolution of 10 degree longitude.

(4) 15 years (1979-1993) of daily ECMWF reanalysis data. The variables used include upper air wind, geopotential height, and temperature. The horizontal resolution is 2.5 degree longitude by 2.5 degree latitude. We average the data along the equator (between 5N and 5S) to pentad data with a zonal resolution of 10 degree longitude.

(5) 24 years (1979-2002) of pentad CMAP precipitation calculated by Xie and Arkin (1997). The horizontal resolution is 2.5 degree longitude by 2.5 degree latitude. We average the data along the equator (between 5N and 5S) with a zonal resolution of 5 degree longitude.

Zonal momentum budget is calculated for both NCEP and ECMWF reanalyses following Carr and Bretherton (2001). The zonal momentum equation can be written:

$$X = \frac{\partial u}{\partial t} + u \frac{\partial u}{\partial x} + v \frac{\partial u}{\partial y} + \omega \frac{\partial u}{\partial p} - f(y)v + \frac{\partial \phi}{\partial x} \quad (1)$$

where u is the zonal wind, v the meridional wind, ω the vertical pressure velocity; x and y are E-W and N-S distance, f the Coriolis parameter, and ϕ the geopotential.

Here X represents accelerations due to all subgrid-scale processes. In the free troposphere (above the effects of boundary layer turbulence eddies), over the open ocean (away from the effects of topographically induced gravity waves), it is resonable to assume that convective momentum transport is the dominant subgrid-scale process.

Under this assumption, we can write:

$$X = \frac{\partial}{\partial p} \overline{u'\omega'} \quad (2)$$

where the overbar denotes an ensemble average at a given pressure level, and primes denote the local perturbation from the ensemble average. In this way, we define X to be the acceleration of the zonal flow due to convergence of zonal momentum flux. The zonal momentum flux at each level is then obtained by integrating upward from the surface:

$$\overline{u'\omega'}(p) = \overline{u'\omega'}_{sfc} - \int_p^{p_{sfc}} X(p) dp \quad (3)$$

Each budget term of Eq. 1 was calculated using daily data at each 2.5 degree longitude by 2.5 degree latitude grid. Derivatives were evaluated using central difference scheme. The results were then averaged to pentad data over a 10 degree longitude by 10 degree latitude box between 150E-160E and 5N-5S. Calculation was done for 15 years (1979-1993) of data for both NCEP and ECMWF reanalyses. Fig. 3 shows profiles of the budget terms averaged over the 15 year period. The Coriolis force is small and is not shown. The 15-year mean pressure gradient force (Fig. 3a) and advection (Fig. 3b) are similar to the 4-month mean for TOGA COARE IFA calculated by Carr and Bretherton (2001, their Fig. 4). There are substantial differences between NCEP and ECMWF reanalyses, especially for pressure gradient force. These differences propagate to and magnify in the residual term (Fig. 3c) and corresponding implied zonal momentum flux (Fig. 3d). However, the implied zonal momentum fluxes at the tropopause are small for both reanalyses, suggesting that

the zonal momentum budget is self-consistent for both reanalyses (see discussions on this consistency check by Carr and Bretherton 2001, and Zhang and Lin 1997).

Although the two reanalyses have substantial differences in time-mean momentum budget, they are much more consistent in MJO anomalous momentum budget, as will be shown later in section 5.

3. Method

All datasets are filtered using a 30-70 day Murakami (1976) filter, whose response function is shown in Fig. 4. The central frequency correspond to a period of 45 day. The half amplitude is at periods of 30 day and 70 day. An MJO composite is constructed using linear regression with respect to an MJO index. In this study, we use filtered CMAP precipitation as our MJO index. Because the MJO is a large-scale phenomenon dominated by wavenumber 0-6 (Wheeler and Kiladis 1998), the CMAP precipitation has been zonally filtered to keep only wavenumber 0-6. The confidence level of linear correlation is estimated following Oort and Yienger (1996).

4. Observed wave structure of the MJO

4.1 Vertical structure along the equator

Fig. 5 shows the vertical structure of MJO at 0N155E from 21 years of NCEP reanalysis data. The time lag is with respect to the time of maximum precipitation. The time evolution is from the right to the left, showing the local evolution of measured variables as the eastward-moving MJO passes the measurement longitude. The

zonal wind (Fig. 5a) shows a simple two-layer structure with the upper layer out of phase with the lower layer. The zonal wind in the upper layer leads the precipitation by nearly a quarter cycle.

This two-layer structure is well-known from many previous observations (e.g. Madden and Julian 1971, 1972, Weickmann et al. 1985, Knutson and Weickmann 1987). An interesting feature which did not bring much attention is that the maxima of both the two layers are at a very high altitude, not the 850 mb and 200 mb levels used in many previous MJO studies. The maximum of the lower layer is around 600 mb (just below the 0 C level), while that of the upper layer is around 150 mb (just below the tropopause). It means that at the time of maximum precipitation, the zonal inflow is just below the 0 C level, and the zonal outflow is just below the tropopause. Consistent with this inflow-outflow feature, the vertical motion (Fig. 5b) concentrates in the upper troposphere. For clarity, the two-dimensional flow is plotted using arrows in Fig. 5c. This middle troposphere inflow and near tropopause outflow structure are consistent with the top-heavy heating profile shown in Lin et al. (2002).

The vertical motion shows a westward phase tilt with height. It develops first in the lower troposphere, and then shifts upward as it intensifies. This westward phase tilt of vertical motion is consistent with the westward phase tilt of the associated heating anomaly shown in Lin et al. (2002), and may reflect or indicate more shallow convection in the earlier stage, and more stratiform precipitation in the later stage.

The geopotential height (contours in Fig. 5c) also shows a two-layer structure,

with the upper layer out of phase with the lower layer. The node is also at high level around 350 mb, as high as that of the zonal wind. The geopotential height in the upper layer is nearly in phase with the precipitation.

Notice the phase difference between the geopotential height and the zonal wind, which is the main interest of this study. At the upper layer, the geopotential height lags the zonal wind by a quarter cycle. Because for both the zonal wind and the geopotential height the upper layer is out of phase with the lower layer, at the lower layer, the geopotential height also lags the zonal wind by a quarter cycle. This quarter cycle phase difference indicates that the equatorial wave structure of the MJO is not a Kelvin wave.

In summary, the equatorial wave structure of the MJO in the NCEP reanalysis has three characteristics: (1) The flow is middle-troposphere inflow and near tropopause outflow at the time of maximum precipitation. (2) The vertical motion has a westward phase tilt with height. (3) The zonal wind lags the geopotential height by a quarter cycle.

The quarter cycle phase difference is consistent with the results of Kiladis and Weickmann (1992) and Hsu (1996) using the operational analysis data, but inconsistent with the result of Hendon and Salby (1994) using the MSU channel 2 temperature data. Therefore next we use the in situ sounding data to validate the above results. Fig. 6 shows the MJO composite of 21 years of sounding data at Pohnpei. Both the zonal wind (Fig. 6a) and geopotential height (Fig. 6b) have similar pattern as the NCEP reanalysis (Fig. 5), and their phase difference at the upper levels is more than

a quarter cycle, again, consistent with the NCEP reanalysis. Three years of ARM sounding data at Manus Island (Fig. 7) shows similar results, especially the quarter cycle phase difference at the upper levels. Further analysis of the sounding data from other stations (Chuuk, Honiara) gives similar results (not shown). Therefore the in situ sounding data support the NCEP reanalysis composite and the results of Kiladis and Weickmann (1992) and Hsu (1996), but does not support the result of Hendon and Salby (1994).

Why does the MSU channel 2 temperature used by Hendon and Salby (1994) give different result? The answer lies in the vertical structure of the temperature anomaly in the MJO (Fig. 8). Consistent with the geopotential height anomaly (Figs. 5c, 6b, 7b), the temperature anomaly concentrates in the upper troposphere, and is nearly in phase with the precipitation and upward motion. The temperature anomaly in the lower troposphere is very small, and tends to lead that in the upper troposphere. The MSU channel 2 temperature used in Hendon and Salby (1994) has most of its weighting from the lower and middle troposphere (Spencer et al. 1990, their Fig. 1). Therefore, the MSU channel 2 is not suitable for representing the troposphere mean temperature in the MJO.

We do not have access to the MSU channel 2 temperature data, but we have obtained a new version of the MSU temperature which separates the upper troposphere temperature (called MSU34) and the lower troposphere temperature (called MSU23). The weighting function of MSU channel 2 temperature is similar to that of MSU23. Fig. 9 shows the MJO composite of (a) MSU34 and (b) MSU23 at 0N155E. We can

see that MSU34 nearly in phase with the precipitation, which is consistent with the upper troposphere temperature in the sounding data. MSU23 leads the precipitation by more than a quarter cycle, which is similar to the lower troposphere temperature in the sounding data. Therefore, MSU34 is better in representing the upper troposphere temperature anomaly in the MJO.

4.2 Horizontal wave structure

In the previous subsection, we have demonstrated that along the equator both the zonal wind and the geopotential height have a two-layer structure, with the center of the upper layer at 150 mb for both the zonal wind and the geopotential height, and the center of the lower layer at 700 mb for the zonal wind. To put the vertical structure along the equator in a three-dimensional perspective, next we look at the horizontal wave structure at these two layers. Fig. 10 shows the horizontal pattern of the geopotential height anomaly at 150 mb and 700 mb. For clarity, we plot the component symmetric to the equator. The most significant feature of the upper layer wave structure (Fig. 10a) is the strong Rossby gyres in the subtropics. The amplitude of Z anomaly at the centers of the Rossby gyres is four times as large as the maximum amplitude of Z anomaly along the equator. The centers of the anticyclones lag the equatorial precipitation by nearly a quarter cycle, i.e., the precipitation lies at the node between the anticyclones and the cyclones. We'll discuss about these strong Rossby gyres later in section 5. At the lower layer (Fig. 10b), there is no strong Rossby gyre.

4.3 Schematics of the observed wave structure

The observed MJO wave structure is schematically depicted in Fig. 11. It has the following characteristics:

- (1) There are very strong subtropical Rossby gyres in the upper troposphere, but not in the lower troposphere.
- (2) At the equator, consistent with the observed top-heavy heating profile, the inflow is at the middle troposphere and the outflow is near the tropopause.
- (3) The vertical motion has a westward phase tilt with height.
- (4) The equatorial wave structure is different from the Kelvin wave, in that zonal wind leads geopotential height by a quarter cycle.

As discussed in the introduction, the quarter cycle phase difference between zonal wind and geopotential height suggest that some terms other than the local tendency and pressure gradient force also contribute to the zonal momentum budget. In order to know exactly what these “extra” terms are, in the next section we directly examine the zonal momentum budget of the MJO.

5. Zonal momentum budget of the MJO

5.1 Dominant budget terms

From Eq. 1, we can write the MJO anomalous zonal momentum equation:

$$\frac{\partial u'}{\partial t} = -\frac{\partial \phi'}{\partial x} + f(y)v' + \left(-u\frac{\partial u}{\partial x} - v\frac{\partial u}{\partial y} - \omega\frac{\partial u}{\partial p}\right)' + X' \quad (4)$$

where primes denote the MJO anomaly. The MJO zonal momentum budget terms at the equator (averaged between 150E-160E and 5N-5S) are shown in Figs. 12 and 13 for NCEP and ECMWF reanalyses, respectively. The Coriolis force is small near the equator and is not shown. The two different reanalyses show similar patterns for each of the three budget terms, giving us more confidence on the results. Moreover, only signals with correlation above the 95% confidence level are plotted in Figs. 12 and 13. These signals are likely real unless there are systematic errors in the reanalyses which are coherent with the MJO. A surprising finding from Figs. 12 and 13 is that in the upper troposphere, the dominant balance is between the advection terms and the pressure gradient force, and the local tendency is very small. This is fundamentally different from the dominant balance in the Kelvin wave, which is between the local tendency and the pressure gradient force (Matsuno 1966, Lindzen 1967).

The budget residual X' is very small for both reanalyses (Fig. 14), and they show similar patterns for this small residual. The implied momentum flux calculated using Eq. 3 is shown in Fig. 15. The momentum flux below 900 mb is associated with the surface wind stress (cf. Fig. 5a). The flux above 700 mb is presumably associated with deep convection in the MJO. During the convectively active phase, both reanalyses suggest upward convective momentum transport. Because zonal wind decreases with height in the warm pool region, this upward flux means a downgradient momentum transport, which is consistent with the results for time-mean budget (Carr and Bretherton 2001; Fig. 3) and easterly waves (Stevens 1979).

Because the advective tendency is one of the two dominant budget terms, and

it contains three components: zonal, meridional and vertical advections, in the next section we examine further the contribution of each individual component.

5.2 Advection terms

The three components of the advective tendency $(-u\frac{\partial u}{\partial x})'$, $(-v\frac{\partial u}{\partial y})'$, $(-\omega\frac{\partial u}{\partial p})'$ are shown separately in Figs. 16a-c. The large advection tendency in the upper troposphere is mainly contributed by zonal advection (Fig. 16a) and vertical advection (Fig. 16c), while that in the lower troposphere is mainly contributed by meridional advection (Fig. 16b). In the following we focus on the zonal and vertical advections in the upper troposphere. Each of these components contain both linear and nonlinear effects, which can be decomposed by:

$$(-u\frac{\partial u}{\partial x})' = -\bar{u}\frac{\partial u'}{\partial x} - u'\frac{\partial \bar{u}}{\partial x} + \text{nonlinear terms} \quad (5)$$

$$(-\omega\frac{\partial u}{\partial p})' = -\bar{\omega}\frac{\partial u'}{\partial p} - \omega'\frac{\partial \bar{u}}{\partial p} + \text{nonlinear terms} \quad (6)$$

where overbars denote time-mean. The linear terms were calculated from the corresponding time-mean (15-year mean) and the MJO anomalies, and the nonlinear terms are derived as the residual. The results are shown in Fig. 17 and Fig. 18, for zonal advection and vertical advection, respectively. The zonal advection (Fig. 17) is dominated by the two linear terms, both of which contribute substantially to the budget. The vertical advection (Fig. 18) is also dominated by the linear terms, especially $-\bar{\omega}\frac{\partial u'}{\partial p}$ (Fig. 18a). Therefore, the zonal momentum budget of the MJO is basically linear.

Because the linear advection terms own their existence to the time-mean zonal wind \bar{u} , zonal divergence $\frac{\partial \bar{u}}{\partial x}$, vertical velocity $\bar{\omega}$, and zonal wind shear $\frac{\partial \bar{u}}{\partial p}$. To help understanding the linear advection terms, we plotted the 15 year (1979-1993) climatological mean of vertical velocity, zonal divergence, and zonal wind in Fig. 19. The zonal wind shear is less important (to be discussed shortly) and is not shown. The warm pool region has the strongest climatological deep convection in the world. The deep convection is associated with strong upward motion (Fig. 19a). The vertical velocity profile is very top-heavy, and is therefore associated with strong upper-level zonal divergence concentrating in a thin layer near the tropopause (Fig. 19b). The upper-level zonal wind over the warm pool is easterly (Fig. 19c), which is presumably associated with the Gill (1980) pattern associated with a stationary heating source. The wind is strong within a thin layer near the tropopause because the zonal divergence is concentrated in this layer. Fig. 19 only shows the annual mean, so the upper-level upward motion and zonal divergence are weaker over the eastern Indian Ocean. Long-term composite seasonal variation of upper-level vertical velocity, zonal divergence, and zonal wind (Fig. 20) show that they are actually very strong over the eastern Indian Ocean during northern summer.

When the MJO travels in such a large-scale environment, $-\bar{u}\frac{\partial u'}{\partial x}$ (Fig. 17a) lags u' (Fig. 5a) by a quarter cycle because of the time-mean upper-levels easterly wind over the warm pool (Fig. 19c). $-u'\frac{\partial \bar{u}}{\partial x}$ (Fig. 17b) is out of phase with u because of the time-mean upper level zonal divergence over the warm pool (Fig. 19b). $-\bar{\omega}\frac{\partial u'}{\partial p}$ (Fig. 18a). is out of phase with the upper-level u' (Fig. 5a) because zonal wind shear

$\frac{\partial u'}{\partial p}$ is in phase with upper-level u' and the time-mean upward motion (negative $\overline{\omega}$, Fig. 19a).

Why, then, is the local tendency much smaller than the advective tendency? We can understand this using a simple scaling analysis. First let's look at the $-u' \frac{\partial \overline{u}}{\partial x}$ term. The time-mean upper-level zonal divergence $\frac{\partial \overline{u}}{\partial x}$ over the warm pool is about 0.2 day^{-1} (Fig. 19b, 20b), equivalent to a time-scale of 5 days. This is much shorter than the 30-70 days time-scale of the MJO. Therefore, $-u' \frac{\partial \overline{u}}{\partial x}$ is much larger than $\frac{\partial u}{\partial t}$ at the MJO time-scale. Because other linear advection terms enhance the $-u' \frac{\partial \overline{u}}{\partial x}$ term, the total advective tendency (Fig. 12c), when scaled using u' (Fig. 5a), is equivalent to a time-scale of 2-3 days. Therefore, the dominant balance between advective tendency and pressure gradient force is a physically robust feature for the MJO.

In summary, the advective tendency is dominated by the linear terms associated with time-mean zonal and vertical motions, including $-\overline{u} \frac{\partial u'}{\partial x}$, $-u' \frac{\partial \overline{u}}{\partial x}$ and $-\overline{\omega} \frac{\partial u'}{\partial p}$. The MJO zonal momentum budget equation Eq. 4 can be simplified to:

$$\frac{\partial u'}{\partial t} = -\frac{\partial \phi'}{\partial x} - \overline{u} \frac{\partial u'}{\partial x} - u' \frac{\partial \overline{u}}{\partial x} - \overline{\omega} \frac{\partial u'}{\partial p} \quad (7)$$

Determined by the strong climatological deep convection over the warm pool, both $-u' \frac{\partial \overline{u}}{\partial x}$ and $-\overline{\omega} \frac{\partial u'}{\partial p}$ are out of phase with u' , making the total advective tendency out of phase with u' . Because the pressure gradient force nearly balances the advective tendency, and is thus in phase with u' , Z' lags u' by a quarter cycle.

The contribution of advective tendency is only large at the equator. Budget calculations for a box off the equator (not shown) indicate that advective tendency becomes

small because of the lack of time-mean upper-level upward motion, zonal divergence and easterly wind off the equator. The dominant balance is geostrophic balance, i.e., between Coriolis force and pressure gradient force.

6. Summary and discussions

This study examined the equatorial wave structure and zonal momentum budget of the MJO. The main findings are twofold.

First, the equatorial wave structure of the MJO is different from the Kelvin wave, in that upper-level zonal wind leads geopotential height by a quarter cycle. The observed wave structure is schematically shown in Fig. 11.

Secondly, the dominant balance in zonal momentum budget is between advective tendency and pressure gradient force. The local tendency is small, as well as the convective momentum flux convergence suggested by budget residual. The advective tendency is dominated by the linear terms associated with time-mean zonal and vertical motions. Simple scaling analysis shows that over the warm pool region, the time-mean upper-level easterly wind, zonal divergence, and upward motion are bound to cause an advective tendency much larger than the local tendency at the MJO time-scale. The simplified MJO zonal momentum equation is Eq. 7.

The above results suggest that the linear advection terms associated with time-mean flow must be included when modeling the MJO wave structure. The WISHE models (Emanuel 1987, Neelin et al. 1987) included the $-\overline{u}\frac{\partial u'}{\partial x}$ term. As discussed in section 5.2, although this term contributes significantly to the total advective

tendency, it is not the cause of the quarter-cycle phase difference between u' and Z' . $-u'\frac{\partial \bar{u}}{\partial x}$ and $-\bar{\omega}\frac{\partial u'}{\partial p}$ must be included in order to simulate the observed quarter-cycle phase difference between u' and Z' . Some of the theoretical models of the MJO included a linear (Rayleigh) damping in the zonal momentum equation, which may be considered as an equivalent of the $-u'\frac{\partial \bar{u}}{\partial x}$ term. When scaled by zonal wind anomaly, the observed advective tendency in the MJO suggests a linear damping time-scale of 2-5 days. Several models using such a strong damping did reproduce the quarter-cycle phase difference between zonal wind and geopotential height at the equator (Chang 1977, Chao 1987, Yamagata 1987). As an example, Fig. 21a shows the horizontal wave structure in the Yamagata (1987) model when the heating moves eastward with the observed MJO phase speed (5 m/s) under a strong damping (nondimensional $\epsilon = 0.25$, which is equivalent to a time-scale of 1 day). At the equator, zonal wind leads geopotential height by a quarter cycle, as in the observation. However, the Rossby response off the equator is significantly reduced by the strong damping. As shown in section 5.2, the observed advective tendency is much smaller off the equator, implying a much weaker damping than at the equator. When we reduce the damping in the model (nondimensional $\epsilon = 0.013$, or a time-scale of 20 day), the Rossby gyres show up (Fig. 21b), which resembles the observation (Figs. 10a), but the equatorial structure becomes like a Kelvin wave. Therefore, if the advective tendency is parameterized as a Rayleigh damping, a latitude-dependent damping coefficient is needed to get the structure correct both at the equator and off the equator.

It will be interesting to study the effect of the quasi-balance between advective

tendency and pressure gradient force on the MJO wave dynamics. Quasi-balanced conditions were shown to be useful for simplifying the basic framework of large-scale dynamics (e.g. Sobel and Bretherton 2000, Bretherton and Sobel 2003). Using the quasi-balance between advective tendency and diabatic heating in the thermodynamic energy equation, Sobel et al. (2001) derived an eastward-propagating balanced mode resembling the observed MJO. In a numerical model, Raymond (2001) also found a similar eastward-propagating balanced mode. It is interesting to study what modes can arise from the quasi-balance in the momentum equation at the MJO time-scale.

It will also be interesting to study the effect of the observed MJO dynamical structure on the wave-convection feedback mechanisms. A key factor for wave-convection feedback is the phase difference between temperature and the feedback heating component (e.g. surface heat flux, boundary layer moisture convergence, etc.). In the Kelvin wave (Fig. 1, temperature is in phase with upper-level zonal wind, while in the observed MJO (Fig. 11), it is shifted westward for a quarter cycle by the advective tendency. This westward phase shift changes, for example, the role of WISHE to the wave instability. The original WISHE theory (Emanuel 1987, Neelin et al. 1987) was developed in the context of Kelvin wave (Fig. 1). The time-mean surface zonal wind was assumed to be easterly, then the surface flux positive anomaly locates at the surface easterly anomaly, which is in phase with the temperature anomaly and therefore amplifies the wave growth. However, later observations showed that the surface flux positive anomaly locates at the surface westerly which slightly lags the precipitation (e.g. Hendon and Glick 1997). Then in the context of Kelvin wave, the

surface flux would be negatively correlated with temperature and therefore damps the wave growth. This constituted a major difficulty for the WISHE mechanism when applied to the MJO. This situation is changed when we consider the quarter-cycle westward shift of temperature anomaly in the observed MJO (Fig. 11), which makes the surface flux positively correlated with temperature, and therefore amplify the MJO. In other word, WISHE helps to destabilize the observed MJO. Therefore, it is interesting to study the effect of the strong linear advective tendency in the MJO on the different wave-convection feedback mechanisms.

REFERENCES

- Bergman, J. W., H. H. Hendon, K. M. Weickmann, 2001: Intraseasonal Air-Sea Interactions at the Onset of El Nino. *Journal of Climate*, **14**, 1702-1719.
- Bretherton, C. S., Sobel, A. H. 2003: The Gill Model and the Weak Temperature Gradient Approximation. *J. Atmos. Sci.*, **60**, 451-460.
- Carr, Matthew T., Bretherton, Christopher S. 2001: Convective Momentum Transport over the Tropical Pacific: Budget Estimates. *J. Atmos. Sci.*, **58**, 1673-1693.
- Chang, C. P., 1977: Viscous internal gravity waves and low-frequency oscillations in the tropics. *J. Atmos. Sci.*, **34**, 901-910.
- Chao, W. C., 1987: On the origin of the tropical intraseasonal oscillation. *J. Atmos. Sci.*, **44**, 1940-1949; Corrigendum, 45, 1283.
- Cho, Han-Ru, D. Pendlebury, 1997: Wave CISK of Equatorial Waves and the Vertical Distribution of Cumulus Heating. *J. Atmos. Sci.*, **54**, 2429-2440.
- Crum, F. R., and T. J. Dunkerton, 1992: Analytic and numerical models of wave-CISK with conditional heating. *J. Atmos. Sci.*, **49**, 1693-1708.
- Duchan, C.E., 1979: Lanczos filtering in one and two dimensions. *J. Appl. Meteor.*, **18**, 1016-1022.
- Emanuel, K. A., 1987: An air-sea interaction model of intraseasonal oscillation in the Tropics. *J. Atmos. Sci.*, **44**, 2324-2340.
- Emanuel, K. A., 1993: The effect of convective response times on WISHE modes. *J. Atmos. Sci.*, **50**, 1763-1775.
- Gallus, William A., Johnson, Richard H. 1992: The Momentum Budget of an Intense

- Midlatitude Squall Line. *J. Atmos. Sci.*, **49**, 422-450.
- Gill, A. E., 1980: Some simple solutions for heat-induced tropical circulation. *Quart. J. Roy. Meteor. Soc.*, **106**, 447-462.
- Hayashi, Y., and D. G. Golder, 1993: Tropical 40-50 and 25-30-day oscillations appearing in realistic and idealized GFDL climate models and the ECMWF dataset. *J. Atmos. Sci.*, **50**, 464-494.
- Hendon, Harry H., Glick, John. 1997: Intraseasonal Air-Sea Interaction in the Tropical Indian and Pacific Oceans. *J. Climate*, **10**, 647-661.
- Hendon, H. H., and B. Liebmann, 1990: A composite study of onset of the Australia monsoon. *J. Atmos. Sci.*, **47**, 2227-2240.
- Hendon, H. H., and M. L. Salby, 1994: The life cycle of the Madden-Julian oscillation. *J. Atmos. Sci.*, **51**, 2225-2237.
- Hsu, H.-H., 1996: Global view of the intraseasonal oscillation during northern winter. *J. Climate*, **9**, 2386-2406.
- Kessler, W. S., and M. J. McPhaden, and K. M. Weickmann, 1995: Forcing of intraseasonal Kelvin waves in the equatorial Pacific. *J. Geophys. Res.*, **100**, 10613-10631.
- Kiladis, G. N., and K. M. Weickmann, 1992: Circulation anomalies associated with tropical convection during northern winter. *Mon. Wea. Rev.*, **120**, 1900-1923.
- Kiladis, G. M., and M. Wheeler, 1995: Horizontal and vertical structure of observed tropospheric equatorial Rossby waves. *J. Geophys. Res.*, **100**, 22981-22997.
- Knutson, T. R., and K. M. Weickmann, 1987: The 30-60 day atmospheric oscillation: Composite life cycles of convection and circulation anomalies. *Mon. Wea. Rev.*, **115**,

1407-1436.

Lau, K. M., and P. H. Chan, 1985: Aspects of the 40-50-day oscillation during the northern winter as inferred from outgoing longwave radiation. *Mon. Wea. Rev.*, **113**, 1889-1909.

Lau, K. M., and L. Peng, 1987: Origin of low-frequency (intraseasonal) oscillations in the tropical atmosphere. *J. Atmos. Sci.*, **44**, 950-972.

Lau, K.-M., and T. J. Phillips, 1986: Coherent fluctuations of extratropical geopotential height and tropical convection in intraseasonal timescales. *J. Atmos. Sci.*, **43**, 1164-1181.

Lau, N. C., I. M. Held, and J. D. Neelin, 1988: The Madden-Julian oscillations in an idealized general circulation model. *J. Atmos. Sci.*, **45**, 3810-3831.

Liebmann, B., H. H. Hendon, and J. D. Glick, 1994: The relationship between the tropical cyclones of the western Pacific and Indian Oceans and the Madden-Julian oscillation. *J. Meteor. Soc. Japan*, **72**, 401-411.

Lindzen, R. D., 1967: Planetary waves on beta-planes. *Mon. Wea. Rev.*, **95**, 441-451.

Madden, R. A., and P. R. Julian, 1971: Detection of a 40-50 day oscillation in the zonal wind in the tropical Pacific. *J. Atmos. Sci.*, **28**, 702-708.

Madden, R. A., and P. R. Julian, 1972: Description of global-scale circulation cells in the tropics with a 40-50 day period. *J. Atmos. Sci.*, **29**, 1109-1123.

Madden, R. A., and P. R. Julian, 1994: Observations of the 40-50-day oscillation -A review. *Mon. Wea. Rev.*, **122**, 814-837.

Mapes, B. E., Wu, X. 2001: Convective Eddy Momentum Tendencies in Long Cloud-

- Resolving Model Simulations. *J. Atmos. Sci.*, **58**, 517-526.
- Matsuno, T., 1966: Quasi-geostrophic motions in the equatorial area. *J. Meteor. Soc. Japan*, **44**, 25-43.
- Murakami, M., 1979: Large-scale aspects of deep convective activity over the GATE area. *Mon. Wea. Rev.*, **107**, 994-1013.
- Nakazawa, T., 1986: Mean features of 30-60 day variations as inferred from 8-year OLR data. *J. Meteor. Soc. Japan*, **64**, 777-786.
- Neelin, J. D., I. M. Held, and K. H. Cook, 1987: Evaporation-wind feedback and low-frequency variability in the tropical atmosphere. *J. Atmos. Sci.*, **44**, 2341-2348.
- Neelin, D. J., and J. Yu, 1994: Modes of tropical variability under convective adjustment and the Madden-Julian oscillation. Part I: Analytical theory. *J. Atmos. Sci.*, **51**, 1876-1894.
- Nishi, N., 1989: Observational study on the 30-60 day variations in the geopotential and temperature fields in the equatorial region. *J. Meteor. Soc. Japan*, **67**, 187-203.
- Oort, A. H., and J. J. Yienger, 1996: Observed long-term variability in the Hadley circulation and its connection to ENSO. *J. Climate*, **9**, 2751-2767.
- Raymond, D. J., 2001: A New Model of the Madden-Julian Oscillation. *J. Atmos. Sci.*, **58**, 2807-2819.
- Salby, M. L., and H. H. Hendon, 1994: Intraseasonal behavior of clouds, temperature, and motion in the Tropics. *J. Atmos. Sci.*, **51**, 2207-2224.
- Sobel, Adam H., Bretherton, Christopher S. 2000: Modeling Tropical Precipitation in a Single Column. *J. Climate*, **13**, 4378-4392.

- Sobel, Adam H., Nilsson, Johan, Polvani, Lorenzo M. 2001: The Weak Temperature Gradient Approximation and Balanced Tropical Moisture Waves. *J. Atmos. Sci.*, **58**, 3650-3665.
- Spencer, R. W., J. R. Christy, and N. C. Grody, 1990: Global atmospheric temperature monitoring with satellite microwave measurements: Method and results 1979-84. *J. Climate*, **3**, 1111-1128.
- Stevens, D. E., 1979: Vorticity, momentum, and divergence budgets of synoptic-scale wave disturbances in the tropical eastern Atlantic. *Mon. Wea. Rev.*, **107**, 535-550.
- Takayabu, Y .N., Toshio Iguchi, Misako Kachi, Akira Shibata and Hiroshi Kanzawa, 1999: Abrupt termination of the 1997-98 El Nino in response to a Madden-Julian oscillation. *Nature*, 402, 279-282.
- Weickmann, K. M., G. R. Lussky, and J. E. Kutzbach, 1985: Intraseasonal (30-60 day) fluctuations of outgoing longwave radiation and 250 mb streamfunction during northern winter. *Mon. Wea. Rev.*, 113, 941-961.
- Wheeler, M., and G. N. Kiladis, 1999: Convectively coupled equatorial waves: Analysis of clouds and temperature in the wavenumber-frequency domain. *J. Atmos. Sci.*, **56**, 374-399.
- Wheeler, M., G. N. Kiladis, and P. J. Webster, 2000: Large-scale dynamical fields associated with convectively coupled equatorial waves. *J. Atmos. Sci.*, **57**, 613-640.
- Wu, X., and M. Yanai, 1994: Effect of vertical wind shear on the cumulus transport of momentum: Observations and parameterization. *J. Atmos. Sci.*, **51**, 1640-1660.
- Xie, P., and P. A. Arkin, 1997: Global precipitation: A 17-year monthly analysis based on

- gauge observations, satellite estimates, and numerical model outputs. *Bull. Amer. Meteor. Soc.*, **78**, 2539-2558.
- Yamagata, T., 1987. A simple moist model relevant to the origin of intraseasonal disturbances in the tropics. *J. Meteor. Soc. Japan*, **65**, 153-165.
- Yasunari, T., 1979: Cloudiness fluctuations associated with the northern hemisphere summer monsoon. *J. Meteor. Soc. Japan*, 57, 227-242.
- Zhang, M. H., and J. L. Lin, 1997: Constrained variational analysis of sounding data based on column-integrated budgets of mass, heat, moisture, and momentum: Approach and application to ARM measurements. *J. Atmos. Sci.*, **54**, 1503-1524.

FIGURE CAPTIONS

Fig. 1 Schematic depiction of the convectively coupled Kelvin wave. Regions of enhanced large-scale convection are indicated schematically by the clouds. The dark shading inside the clouds represents the maximum of the diabatic heating. The arrows represent the anomalous wind. “H” and “L” represent the high and low geopotential height anomalies, respectively. “W” inside thick solid circle and “C” inside thick dashed circle represent the warm and cold temperature anomalies, respectively.

Fig. 2 Standard deviation of the 30-70 day bandpass filtered anomaly of the CMAP precipitation from 1979-1999. The unit is mm/day. The thick solid polygons are the sounding arrays during TOGA COARE. The inner one is the Intensive Flux Array (IFA). The outer one is the Outer Sounding Array (OSA).

Fig. 3 Terms of time-mean zonal momentum budget (a) local tendency $\frac{\partial u}{\partial t}$, (b) pressure gradient force $-\frac{\partial \phi}{\partial x}$, and (c) advection terms $(-u\frac{\partial u}{\partial x} - v\frac{\partial u}{\partial y} - \omega\frac{\partial u}{\partial p})$, for 15 years (1979-1993) of NCEP reanalysis data averaged over 150E-160E and 5N-5S. Unit is $ms^{-1}day^{-1}$.

Fig. 4 The response function of the Murakami filter used in this study.

Fig. 5 The vertical structure of the MJO anomaly for (a) zonal wind (m/s), (b) vertical velocity (mb/day), and (c) geopotential height (m) for the 21 years (1979-1999) of NCEP reanalysis data averaged over 150E-160E and 5N-5S. Negative values are shaded. The arrows in (c) are the wind vectors whose horizontal component is the zonal wind, and vertical component the vertical velocity.

Fig. 6 Same as Fig. 5a, b except for 21 years (1979-1999) of sounding data at Pohnpei.

Fig. 7 Same as Fig. 5a, b except for three years (2000-2002) of sounding data at Manus.

Fig. 8 The vertical structure of the MJO temperature anomaly (K) for (a) 21 years (1979-1999) of NCEP reanalysis data at 0N155E, (b) 21 years (1979-1999) of sounding data at Pohnpei, and (c) three years (2000-2002) of sounding data at Manus.

Fig. 9 The temperature anomaly during the life cycle of the MJO for 15 years (1979-1993) of (a) MSU34 data, and (b) MSU23 data averaged over 150E-160E and 5N-5S..

Fig. 10 The horizontal structure of the MJO anomaly for geopotential height (contours; unit m) and wind (vectors) at (a) 150 mb, and (b) 700 mb. Only the component symmetric to the equator is plotted.

Fig. 11 Schematic depiction of the observed MJO wave structure. The middle part of each panel represents wave structure in the equatorial vertical plane. Regions of enhanced large-scale convection are indicated schematically by the clouds. The dark shading inside the clouds represents the maximum of the diabatic heating. The arrows represent the anomalous wind. “H” and “L” represent the high and low geopotential height anomalies, respectively. “W” inside thick solid circle and “C” inside thick dashed circle represent the warm and cold temperature anomalies, respectively. The upper part of each panel is a plan view of the wave at 150 mb centered at the equator. The contours represent the anomalous geopotential height. The arrows represent the anomalous wind. Shading indicates the positive heating anomaly. The lower part of

each panel is the same as the upper part except for 700 mb.

Fig. 12 Terms of the MJO zonal momentum budget: (a) local tendency $\frac{\partial u'}{\partial t}$, (b) pressure gradient force $-\frac{\partial \phi'}{\partial x}$, and (c) advection terms $(-u\frac{\partial u}{\partial x} - v\frac{\partial u}{\partial y} - \omega\frac{\partial u}{\partial p})'$, for 15 years (1979-1993) of NCEP reanalysis data averaged over 150E-160E and 5N-5S. Unit is $ms^{-1}day^{-1}$.

Fig. 13 As in Fig. 12 except for ECMWF reanalysis data.

Fig. 14 As in Fig. 12 except for the residual term X' for (a) NCEP reanalysis, and (b) ECMWF reanalysis.

Fig. 15 As in Fig. 12 except for the momentum flux for (a) NCEP reanalysis, and (b) ECMWF reanalysis. Unit is Nm^{-2} .

Fig. 16 As in Fig. 12 except for three advection terms for NCEP reanalysis data: (a) zonal advection $(-u\frac{\partial u}{\partial x})'$, (b) meridional advection $(-v\frac{\partial u}{\partial y})'$, and (c) vertical advection $(-\omega\frac{\partial u}{\partial p})'$.

Fig. 17 As in Fig. 12 except for three components of the zonal advection term for NCEP reanalysis data: (a) $-\overline{u}\frac{\partial u'}{\partial x}$, (b) $-u'\frac{\partial \overline{u}}{\partial x}$, and (c) higher order terms.

Fig. 18 As in Fig. 12 except for three components of the vertical advection term for NCEP reanalysis data: (a) $-\overline{\omega}\frac{\partial u'}{\partial p}$, (b) $-\omega'\frac{\partial \overline{u}}{\partial p}$, and (c) higher order terms.

Fig. 19 Annual mean (a) ω (mb/day), (b) $\frac{\partial \overline{u}}{\partial x}$ (m/s/day), and (c) u (m/s), for 21 years (1979-1999) of NCEP reanalysis data along the equator (5N-5S).

Fig. 20 Seasonal variation of (a) ω (mb/day) at 300 mb, (b) $\frac{\partial \overline{u}}{\partial x}$ (m/s/day) at 150 mb, and (c) u (m/s) at 150 mb, for NCEP reanalysis data along the equator (5N-5S).

Fig. 21 Horizontal wave structure for the Yamagata (1987) model for $C_0 = 0.1$

under (a) strong damping ($\epsilon = 0.25$), and (b) weak damping ($\epsilon = 0.13$). Contours are pressure perturbation, and arrows are wind vectors.

Convectively coupled Kelvin wave

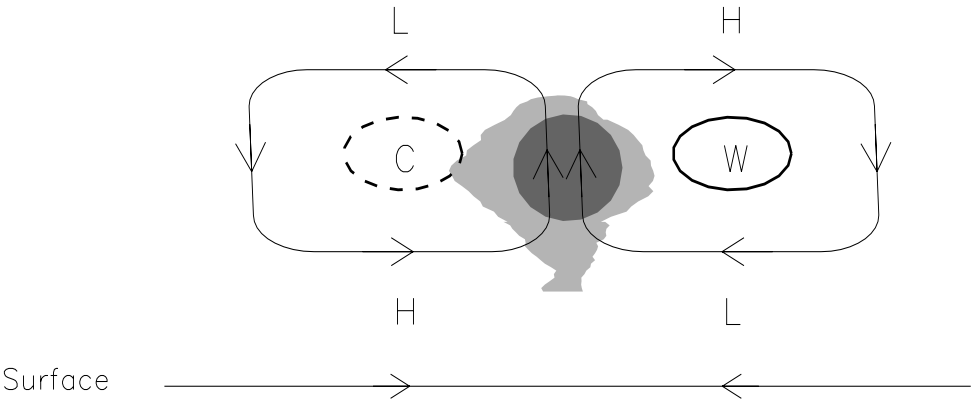


Figure 1:

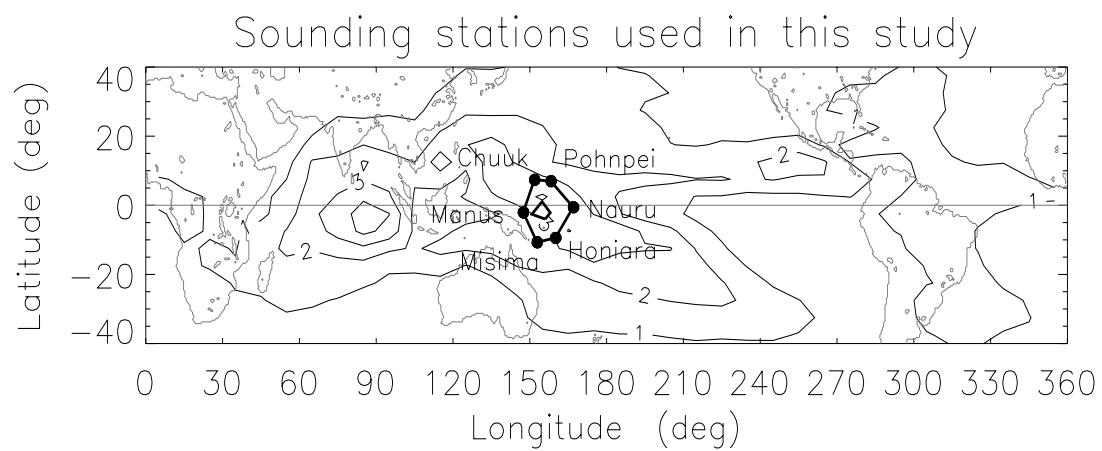


Figure 2:

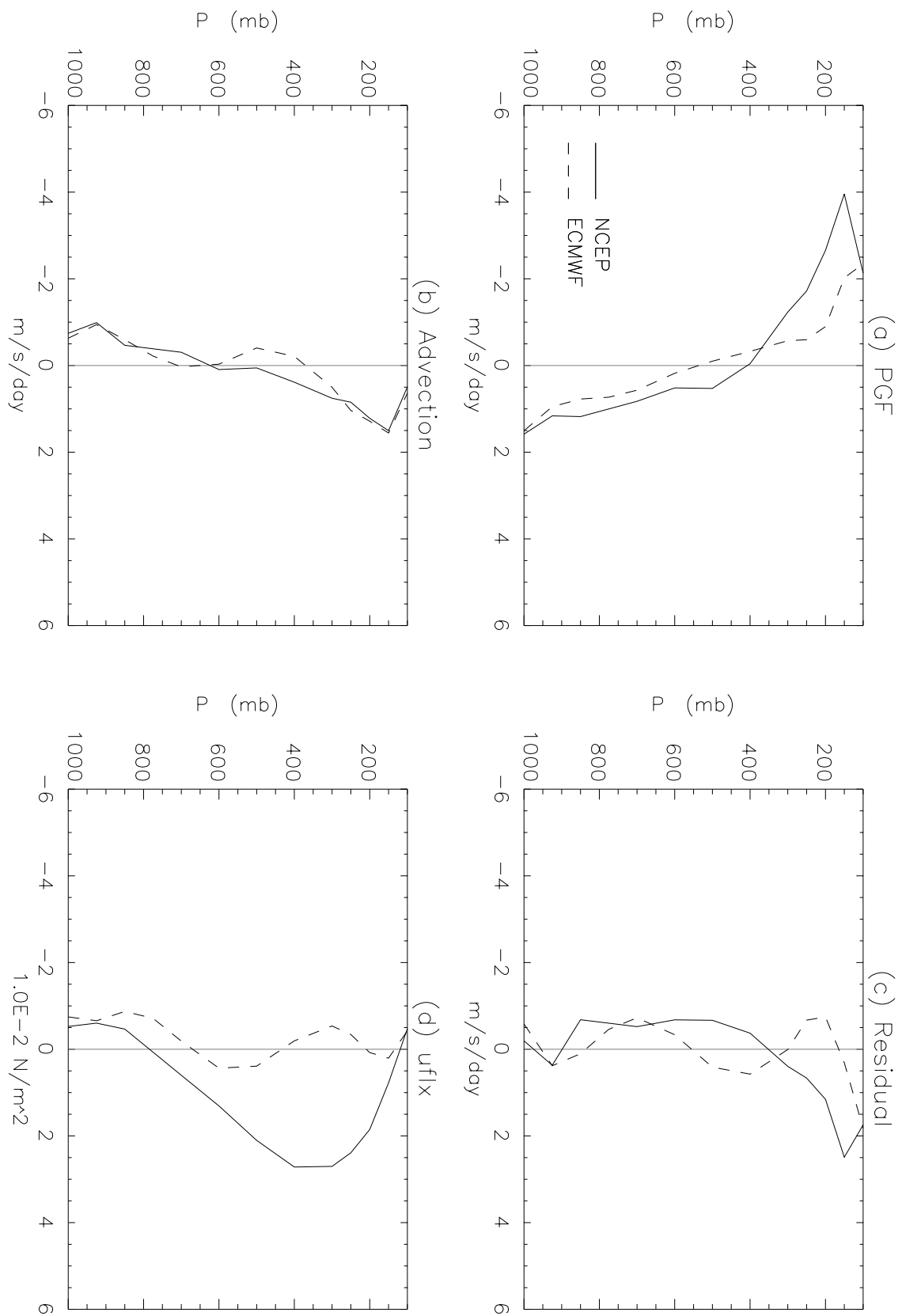


Figure 3:

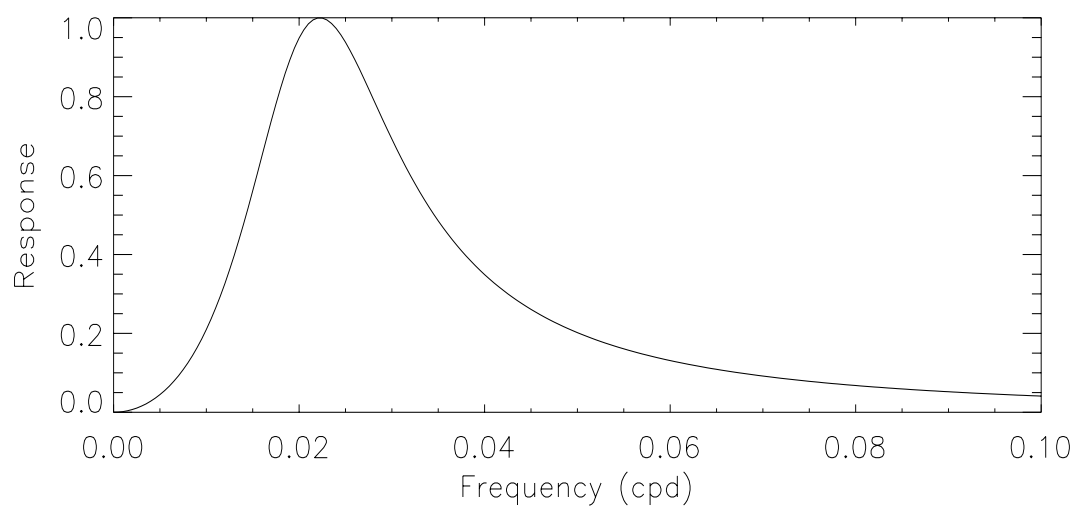


Figure 4:

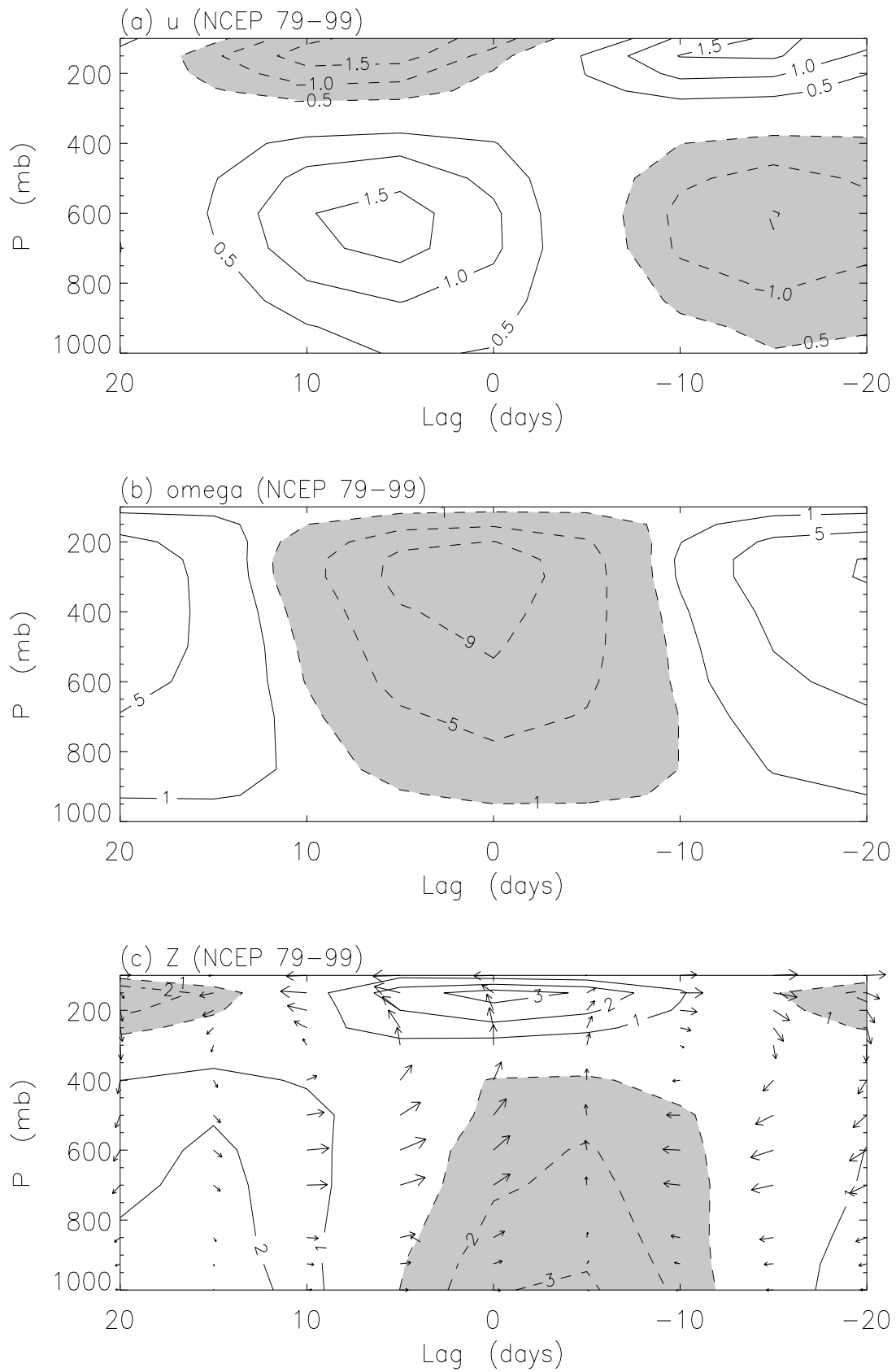


Figure 5:

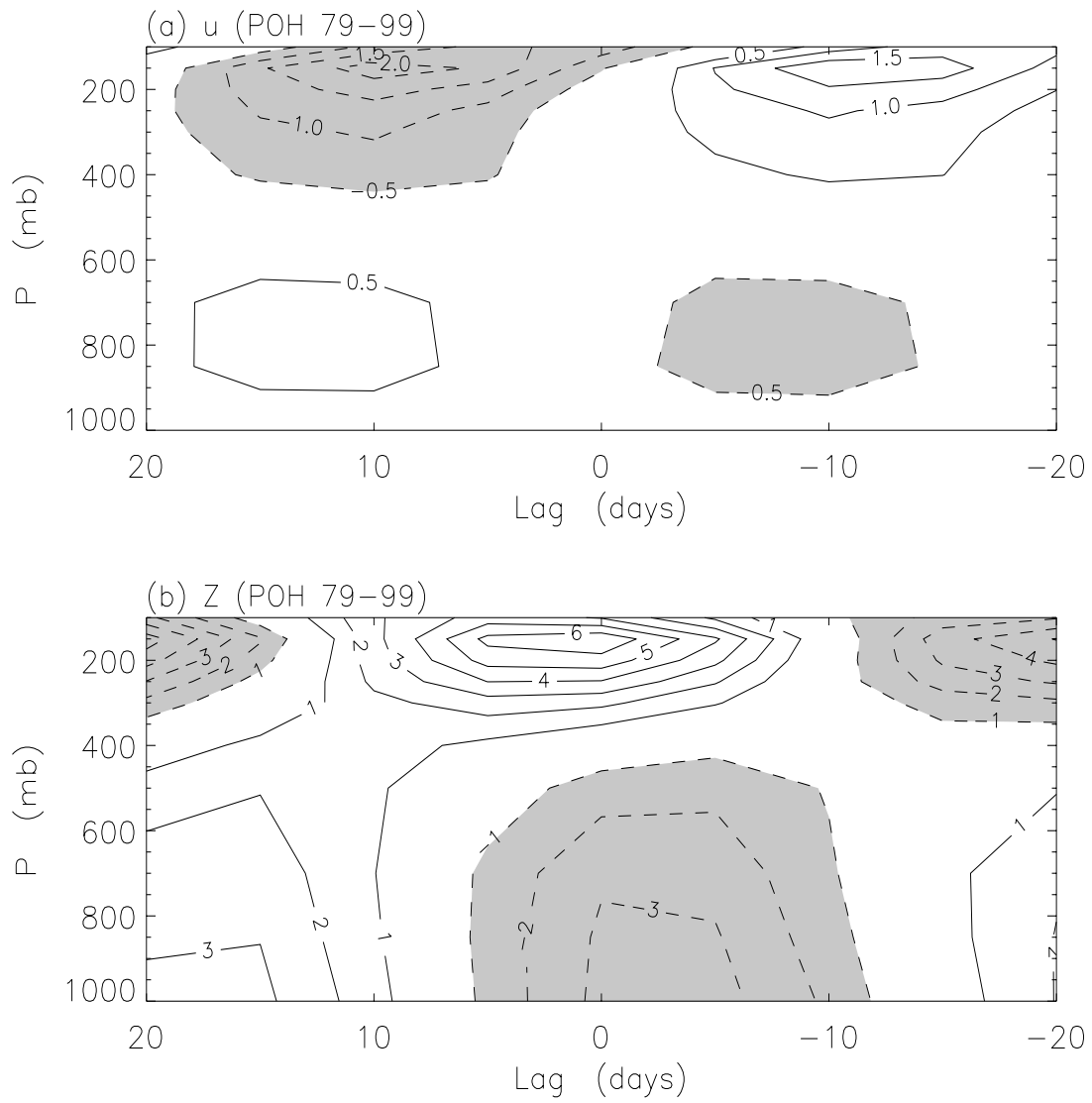


Figure 6:

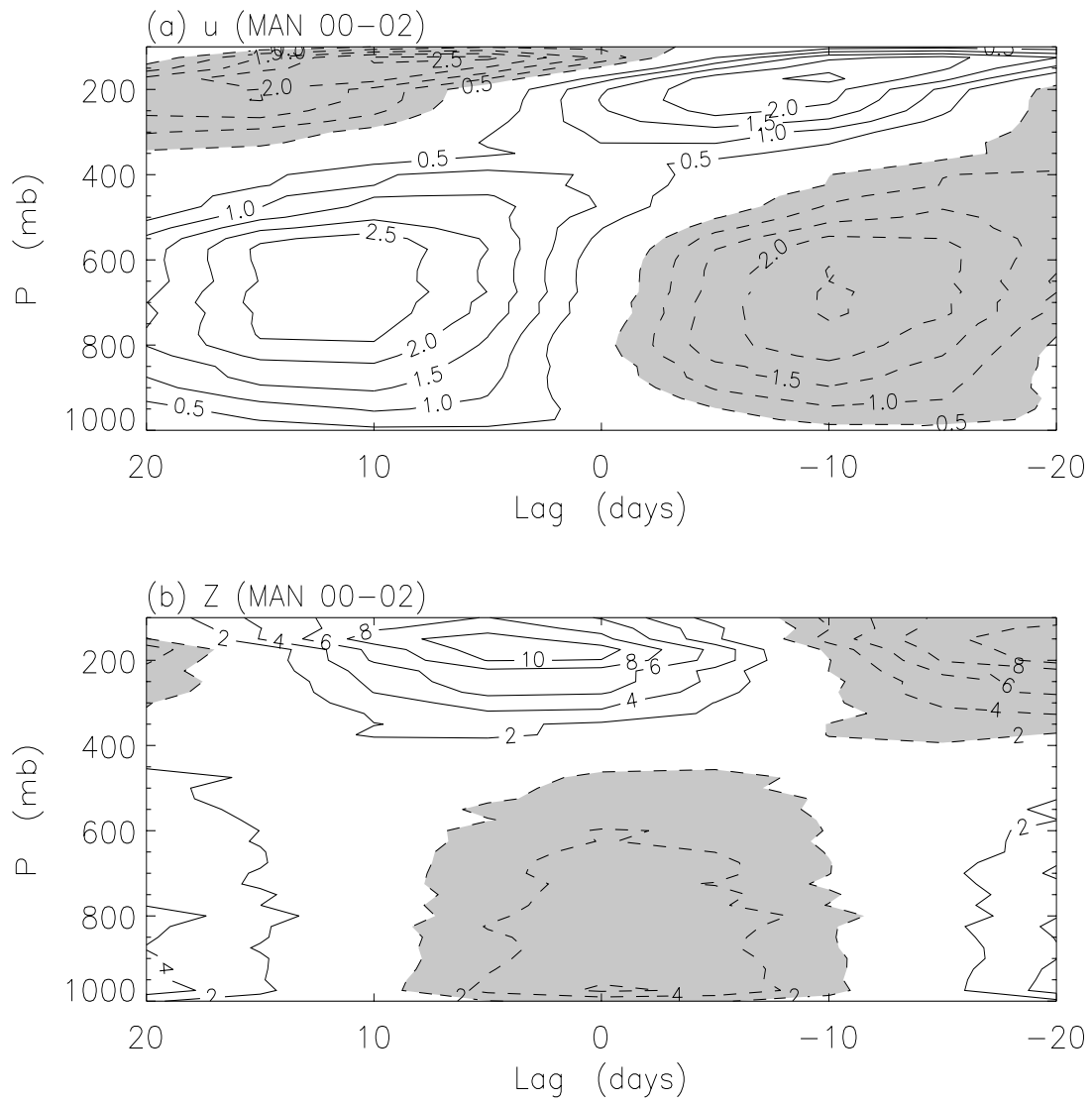


Figure 7:

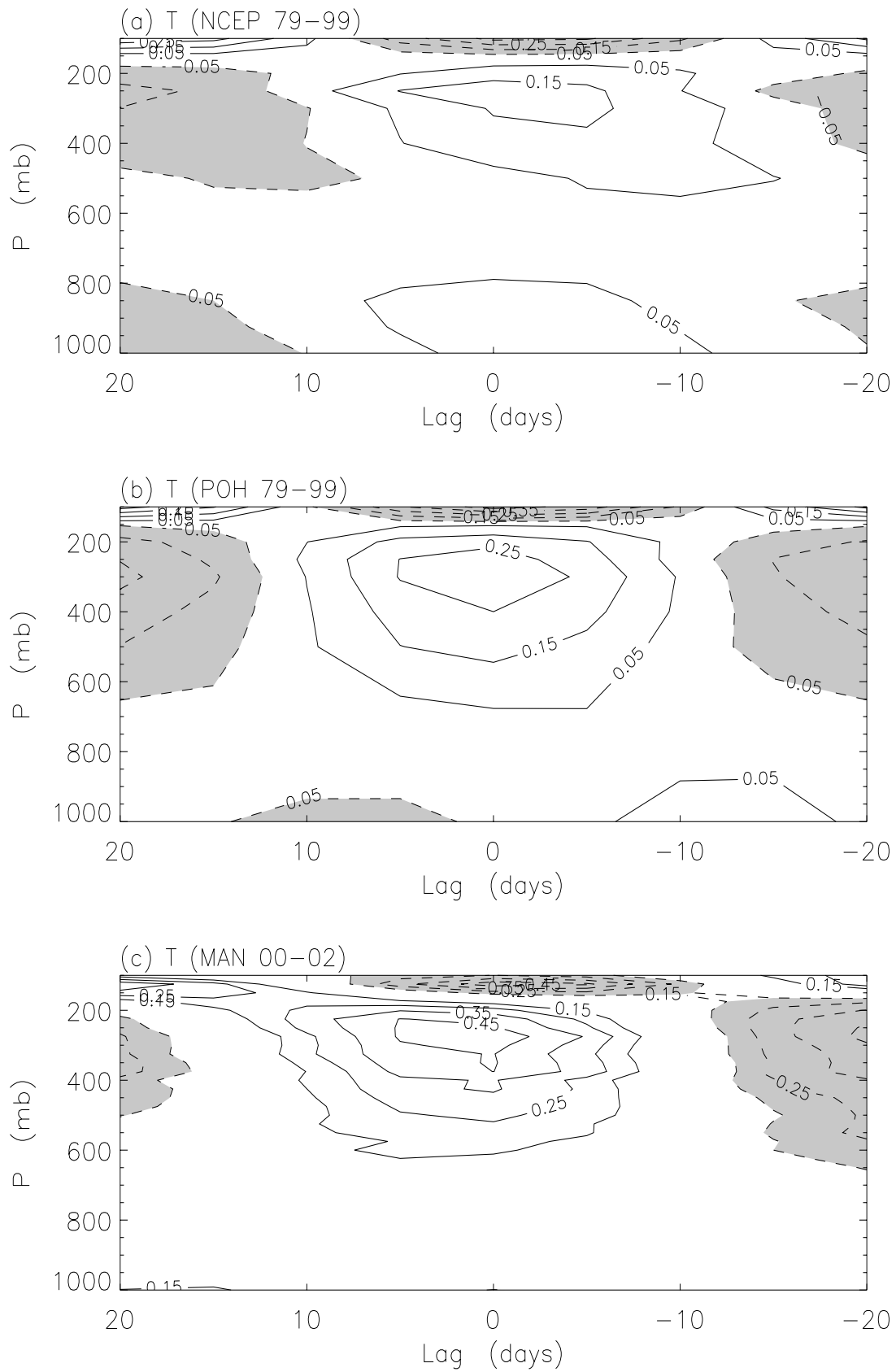


Figure 8:

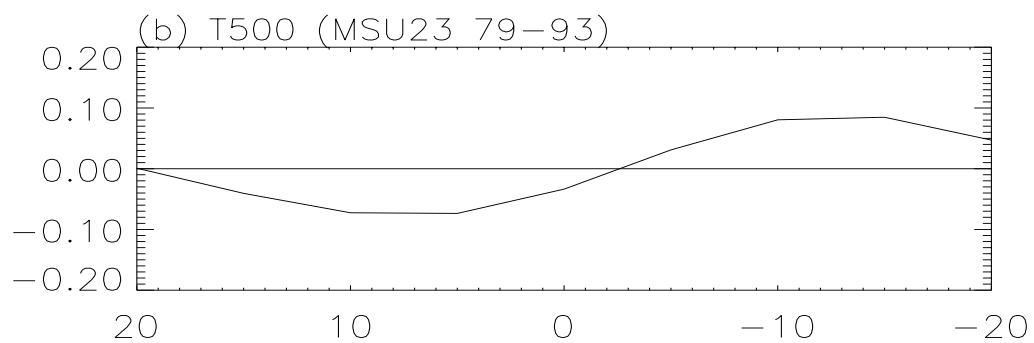
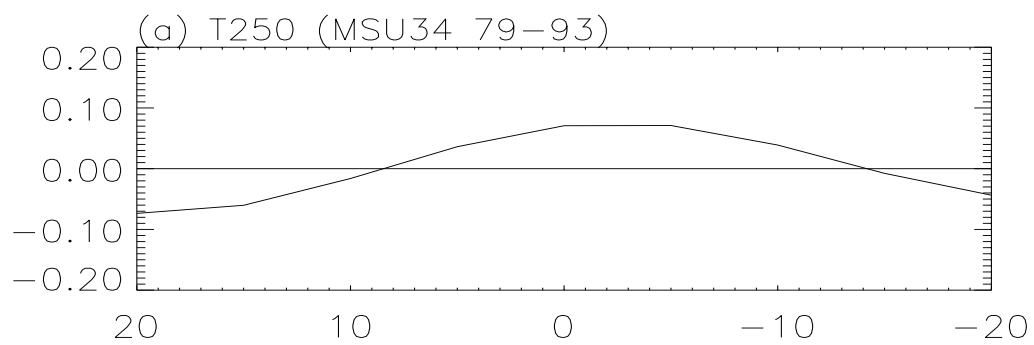


Figure 9:

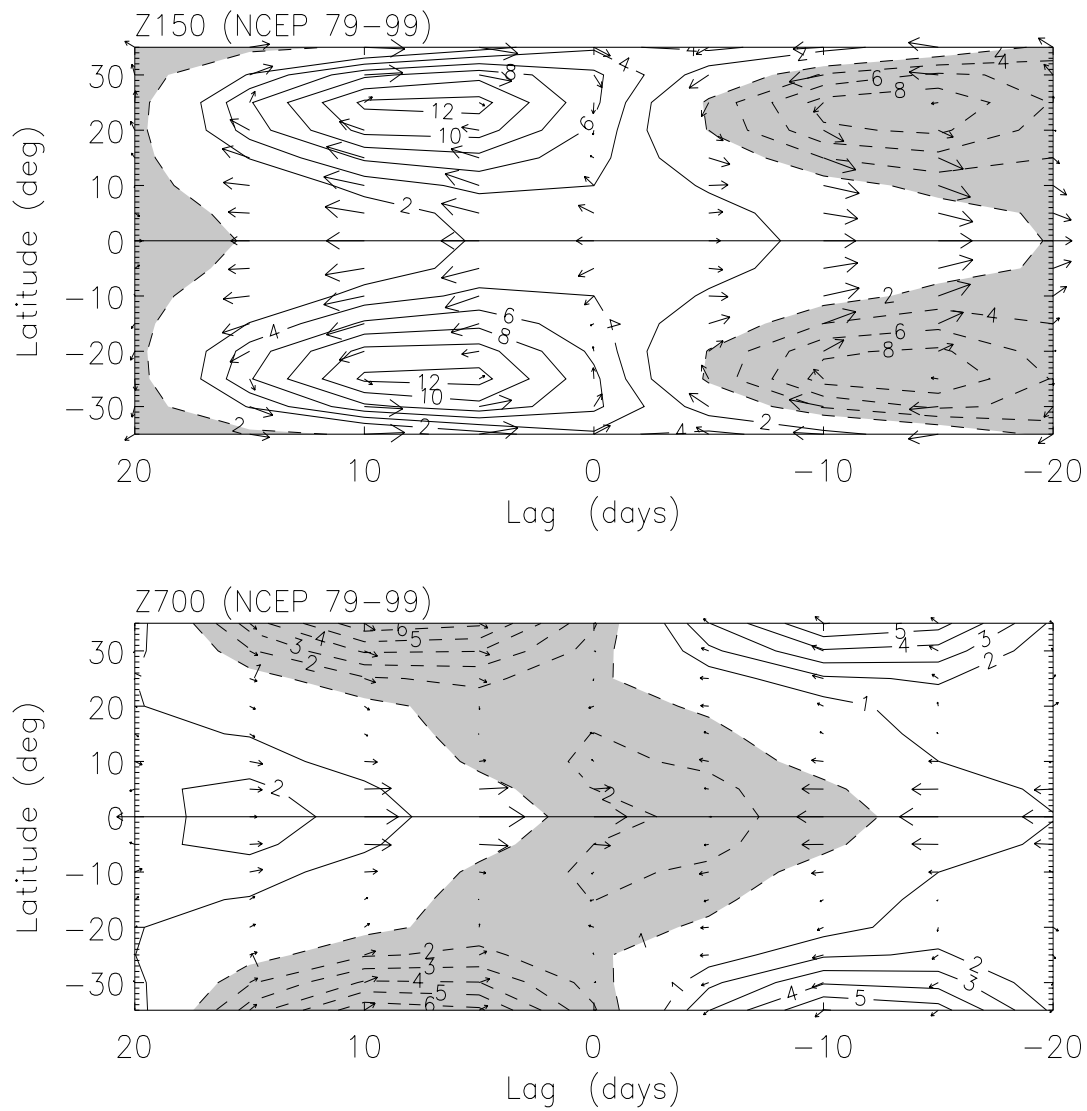


Figure 10:

Observed MJO wave structure

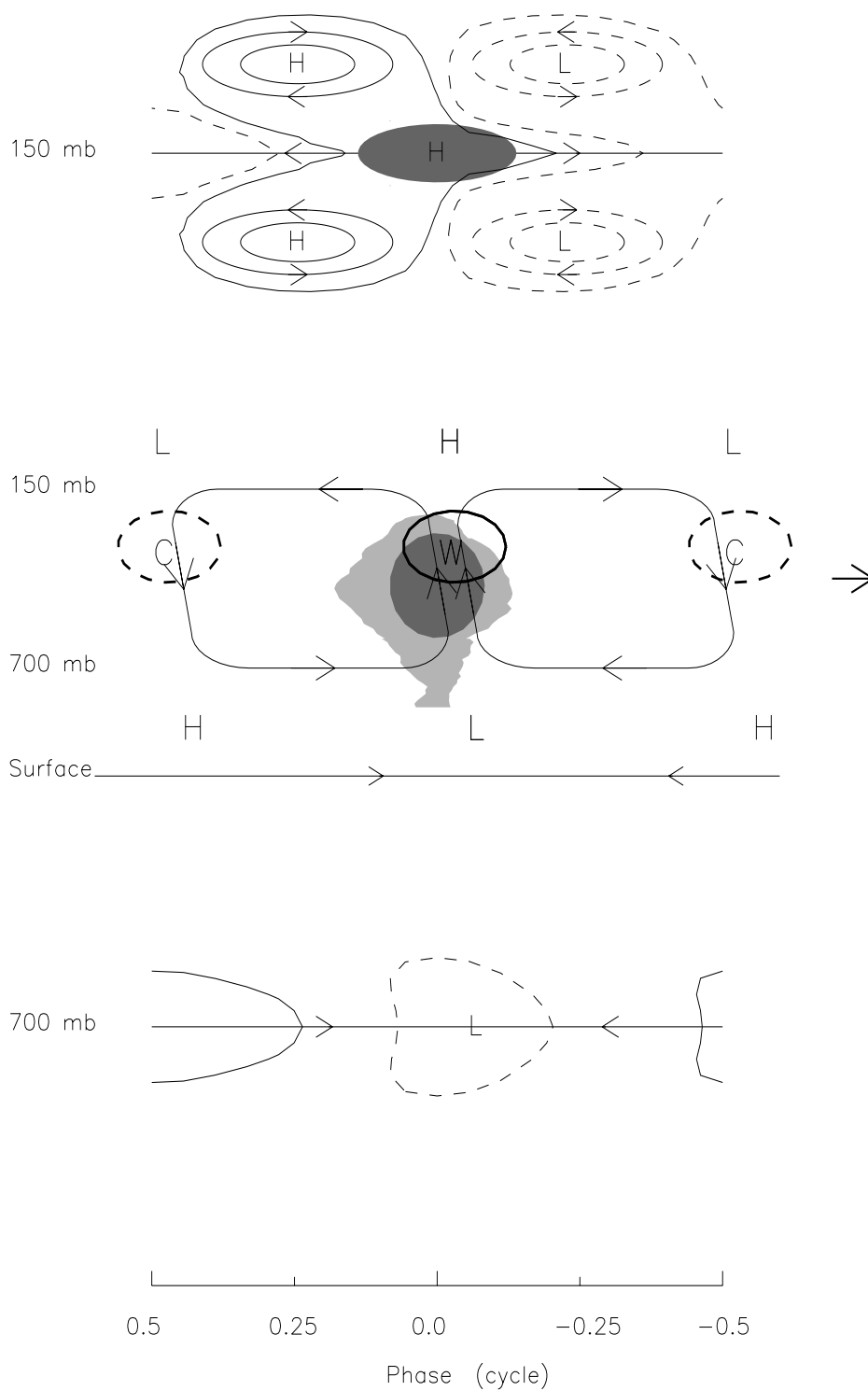


Figure 11:

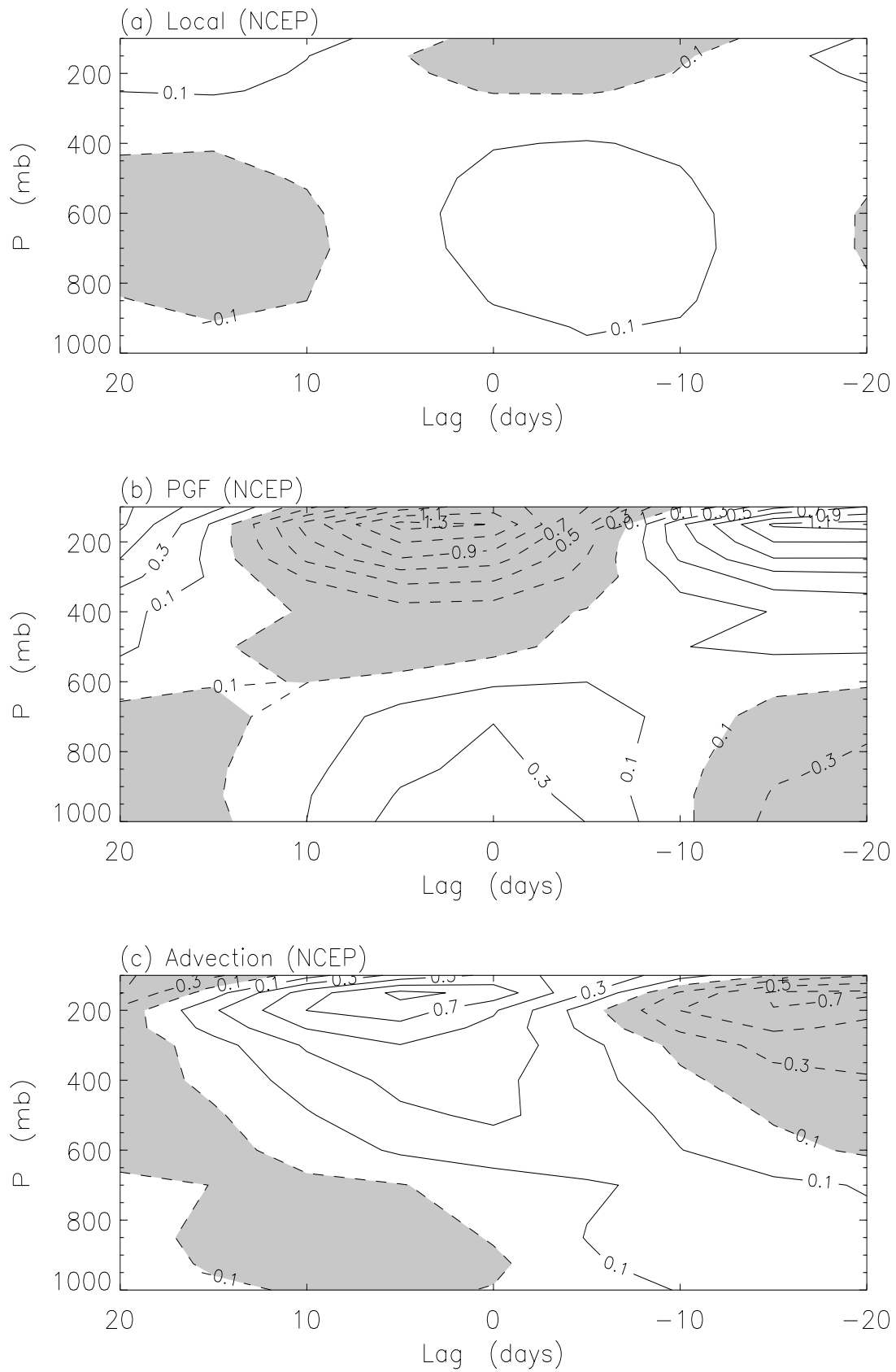


Figure 12:

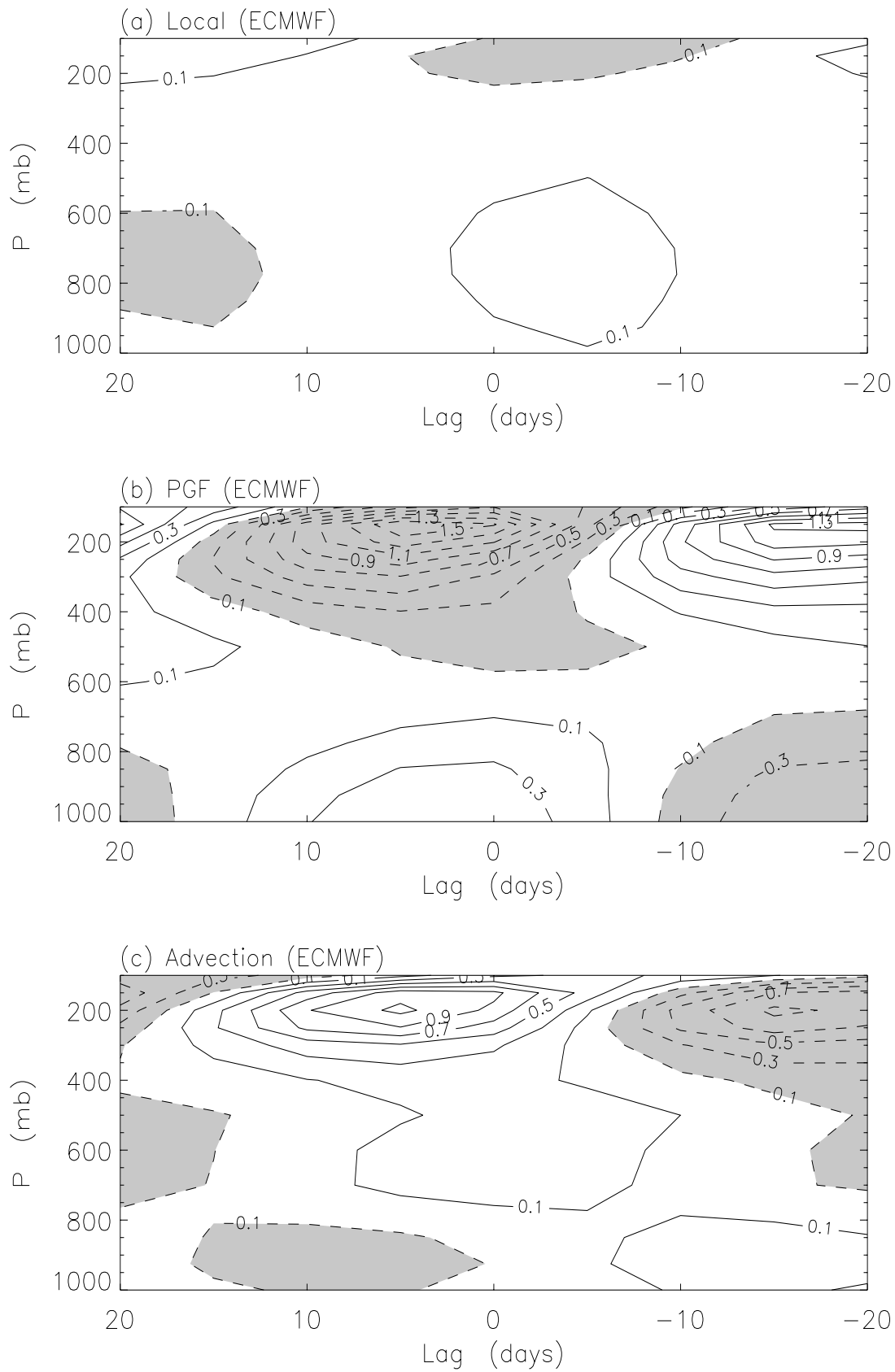


Figure 13:

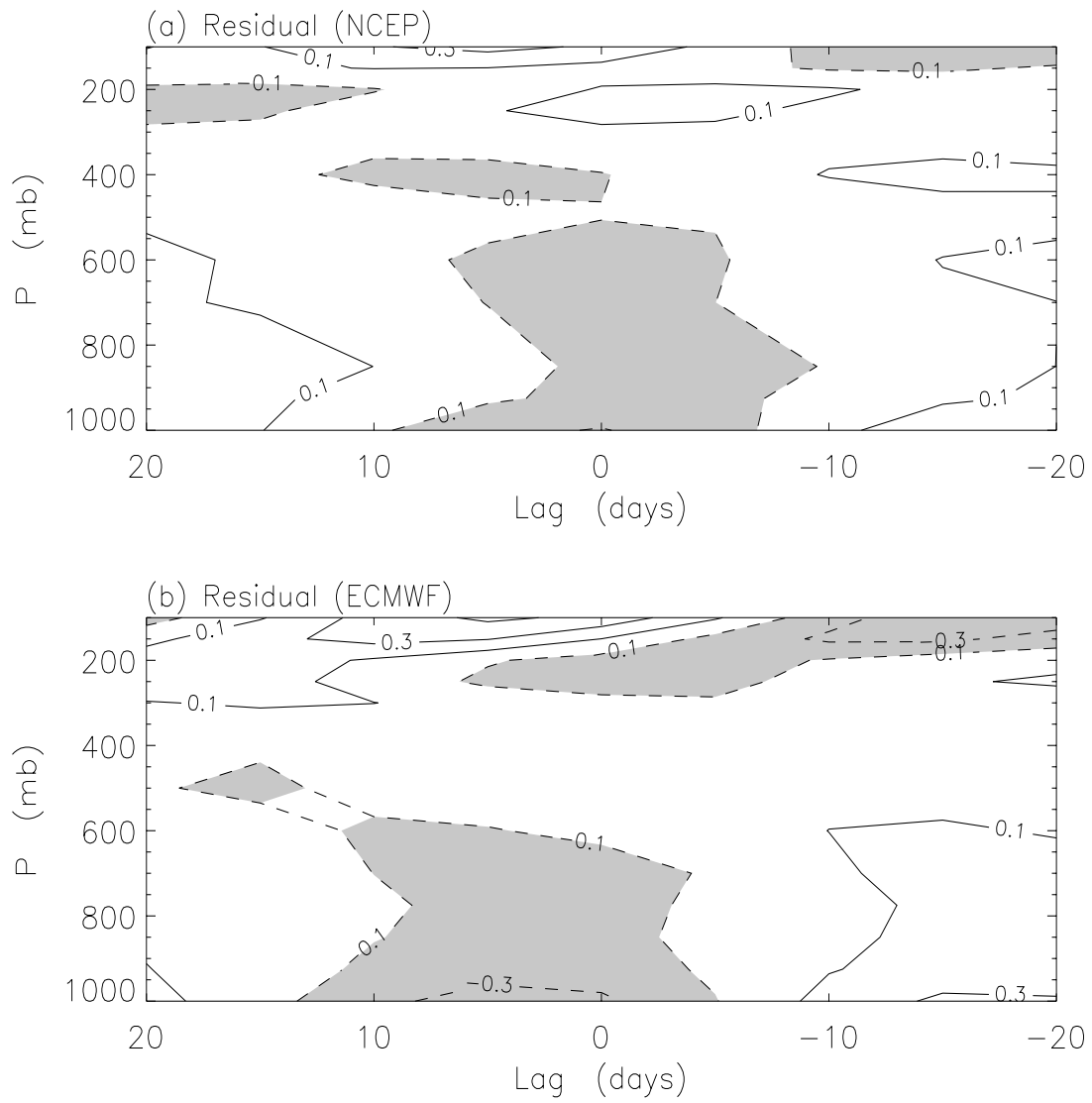


Figure 14:

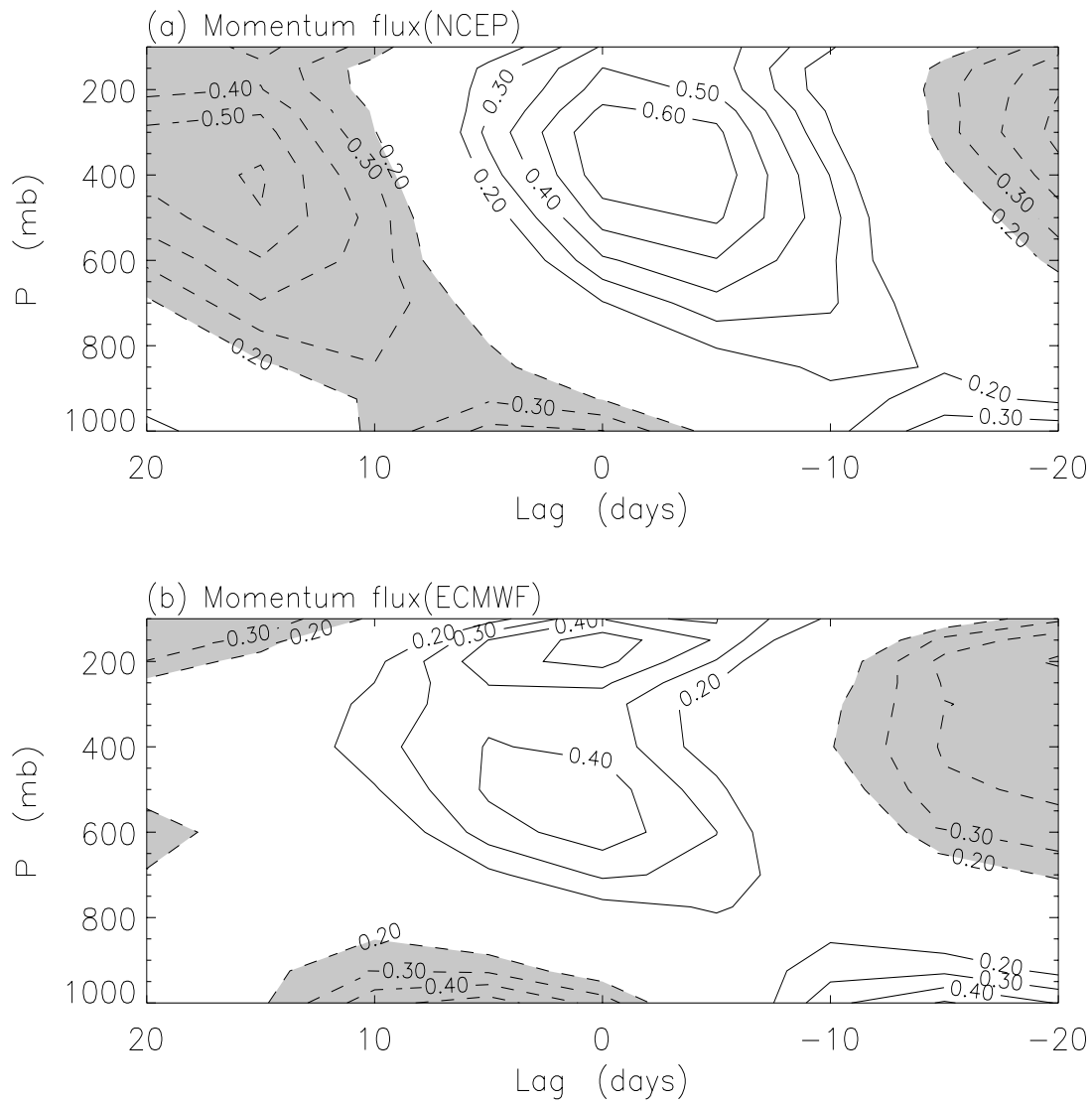


Figure 15:

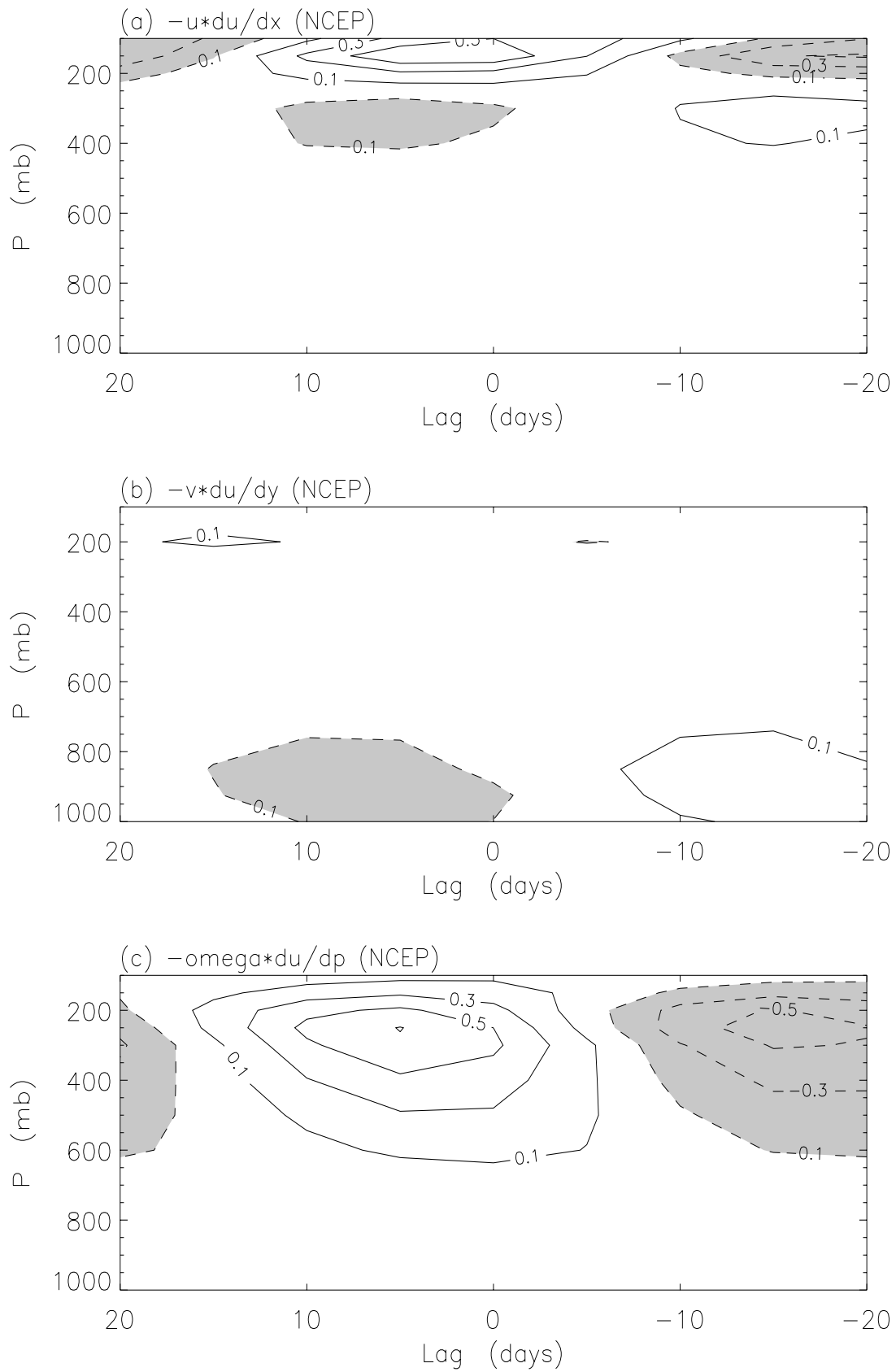


Figure 16:

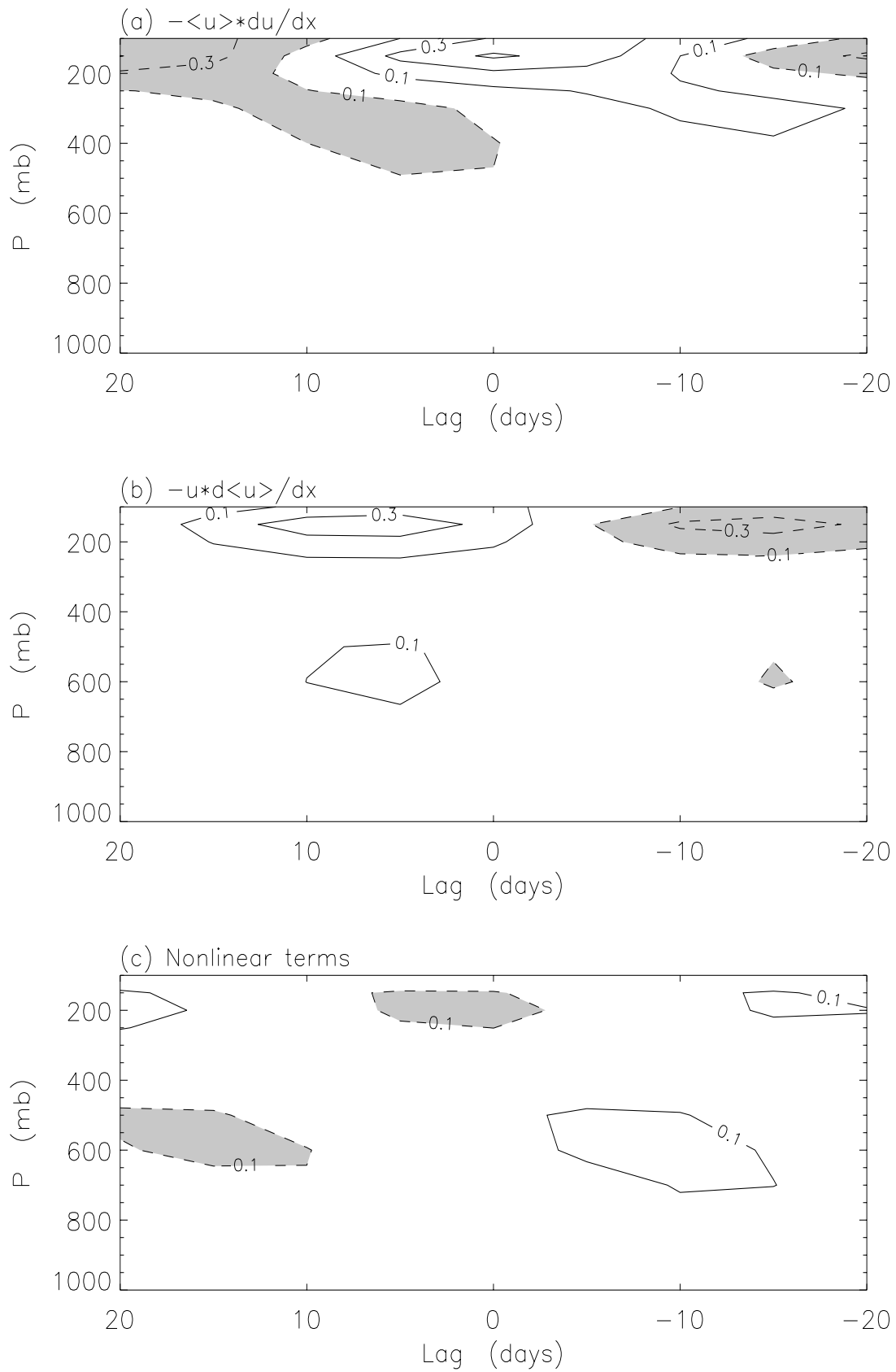


Figure 17:

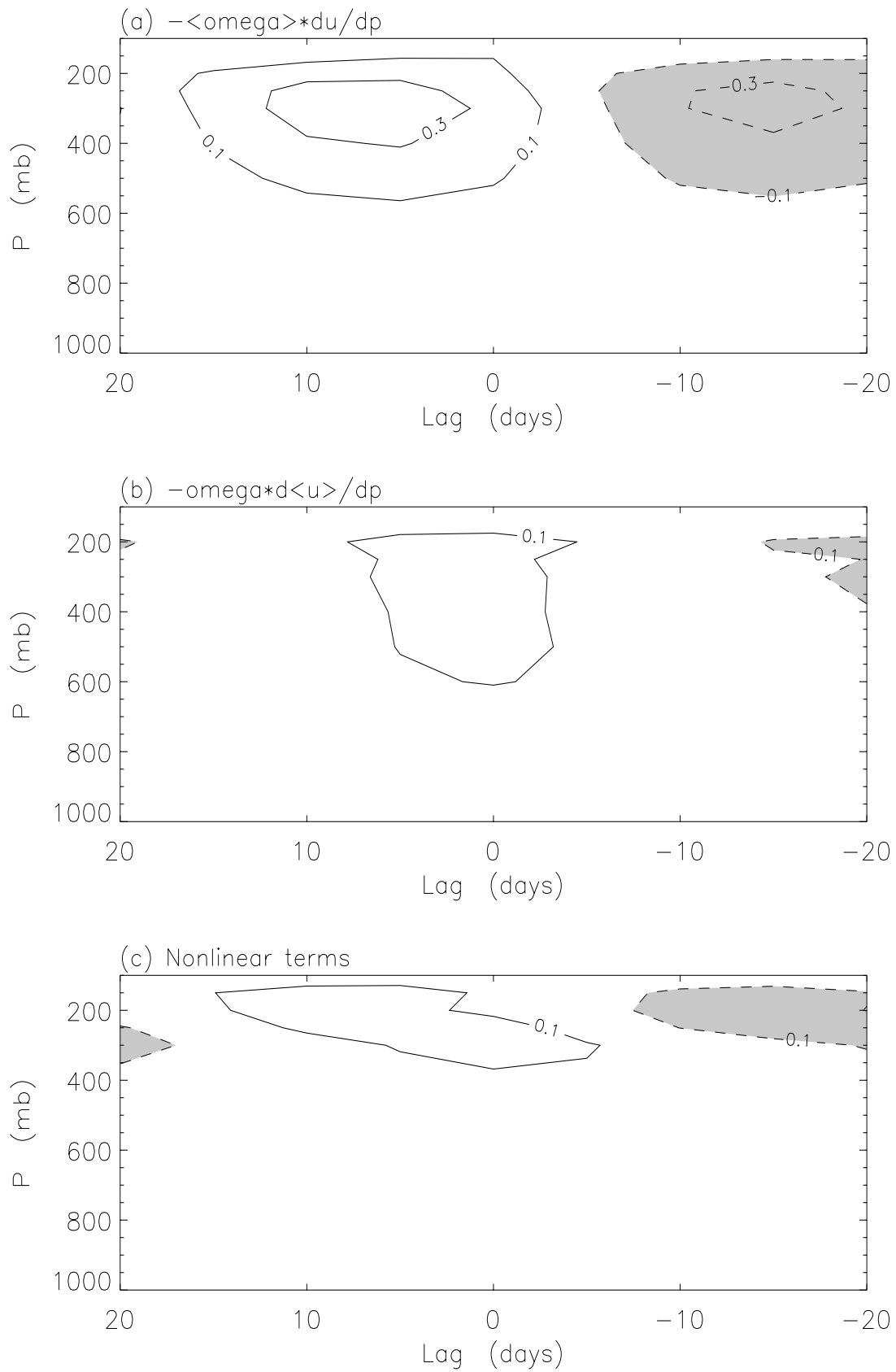


Figure 18:

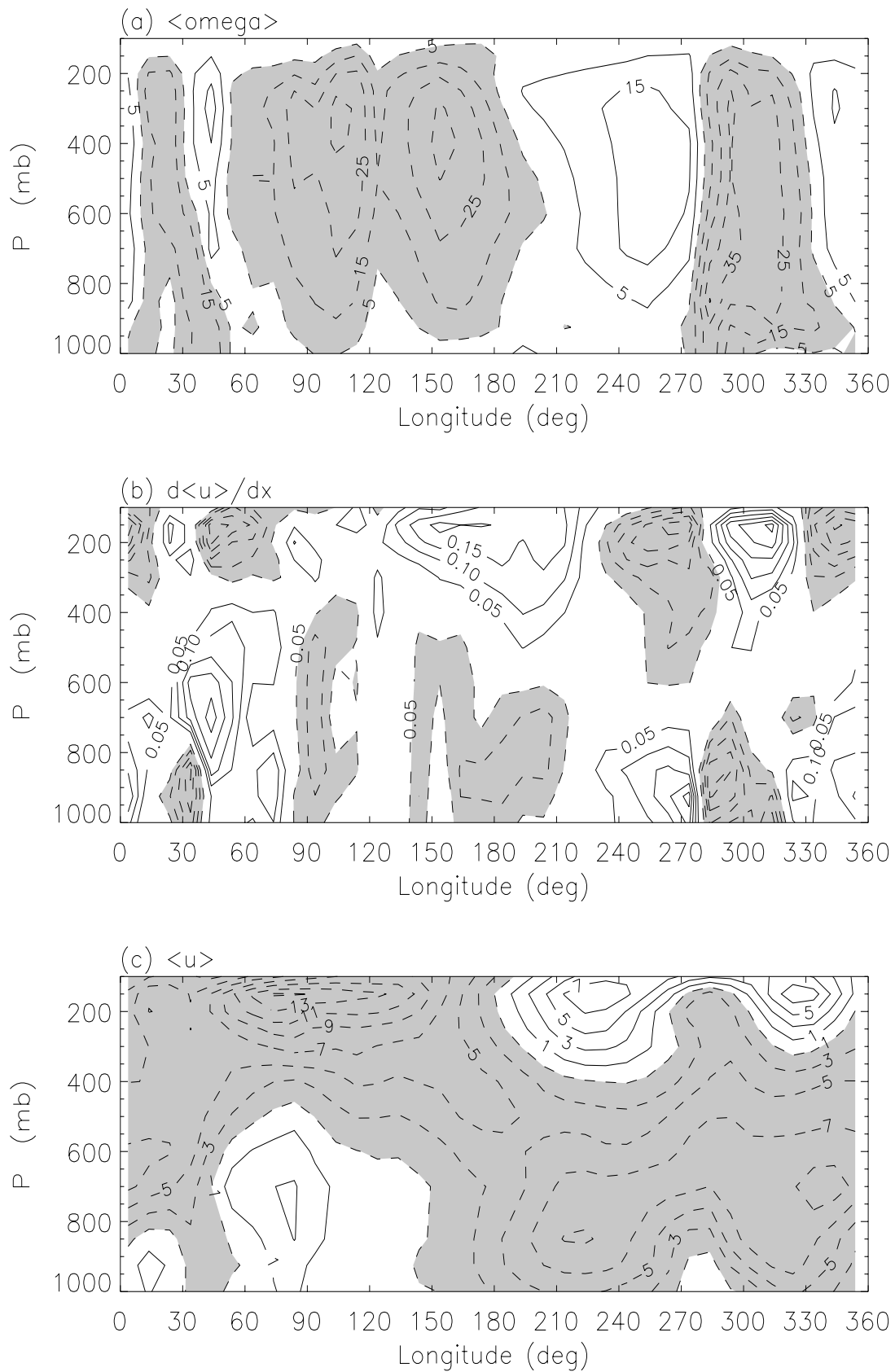


Figure 19:

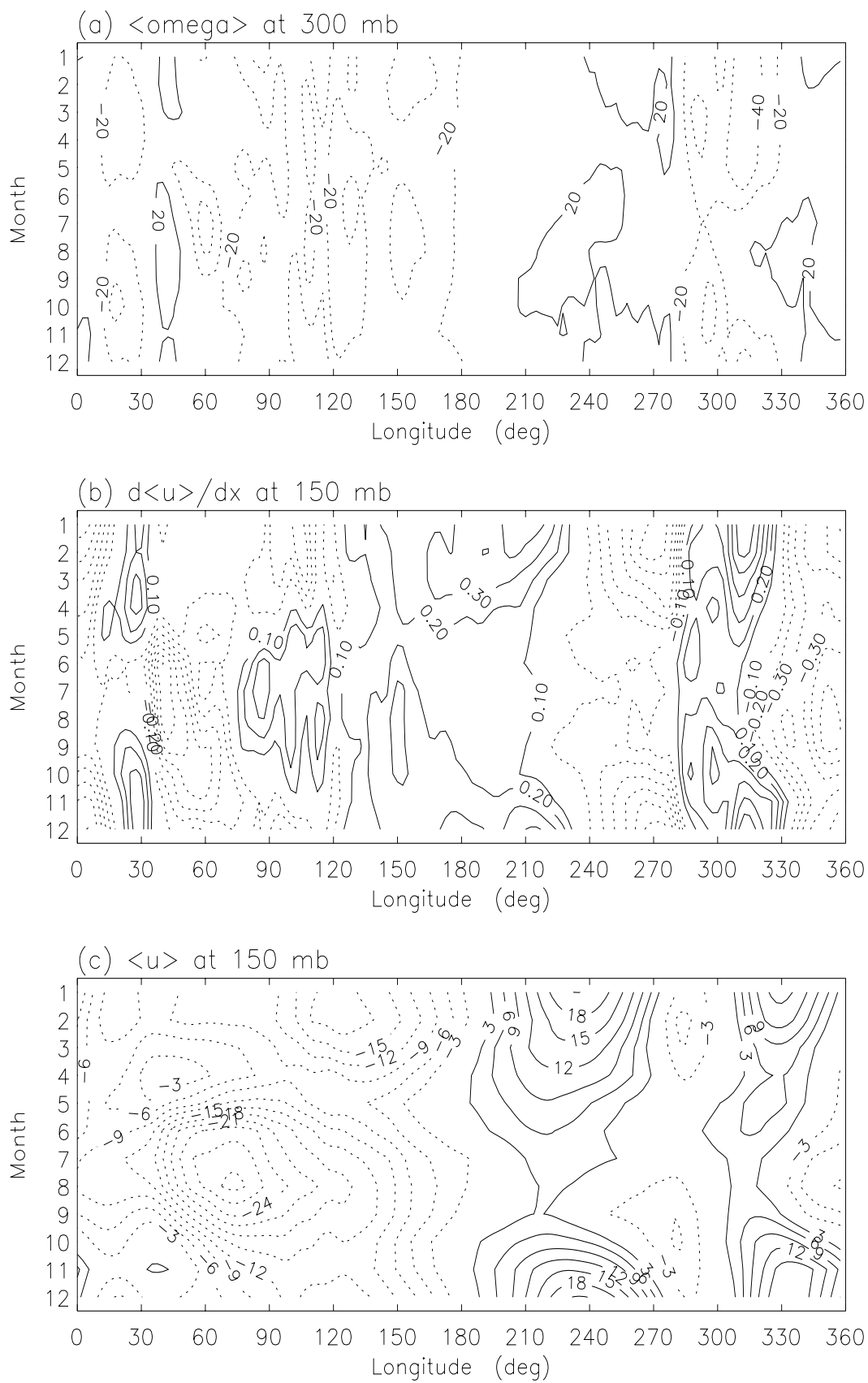


Figure 20:

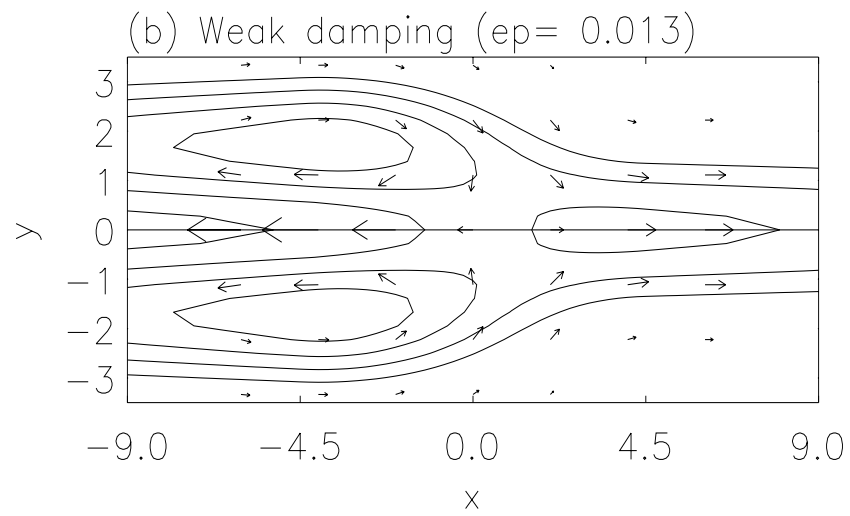
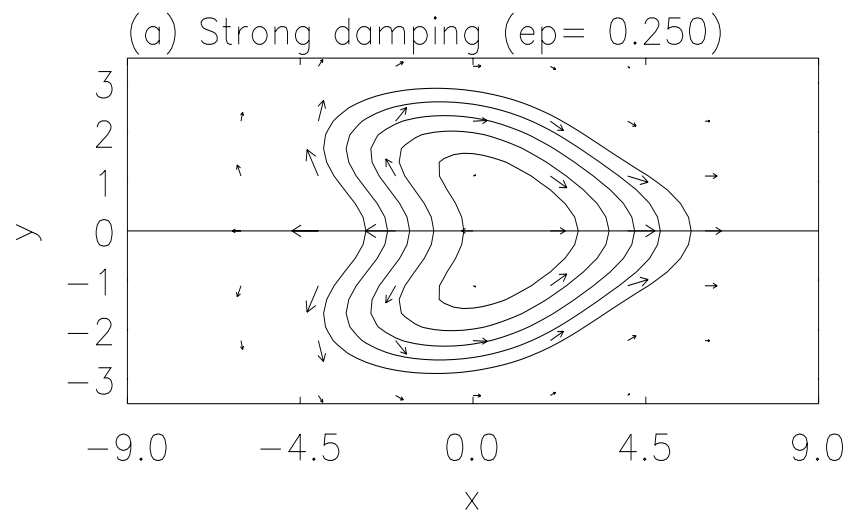


Figure 21: